[American Journal of Science, Vol. 313, March, 2013, P. 145–198, DOI 10.2475/03.2013.01]

American Journal of Science

MARCH 2013

HELIUM DIFFUSION IN NATURAL ZIRCON: RADIATION DAMAGE, ANISOTROPY, AND THE INTERPRETATION OF ZIRCON (U-Th)/He THERMOCHRONOLOGY

WILLIAM R. GUENTHNER*,†, PETER W. REINERS*, RICHARD A. KETCHAM**, LUTZ NASDALA***, and GERALD GIESTER***

ABSTRACT. Accurate thermochronologic interpretation of zircon (U-Th)/He dates requires a realistic and practically useful understanding of He diffusion kinetics in natural zircon, ideally across the range of variation that characterize typically dated specimens. Here we present a series of date and diffusion measurements that document the importance of alpha dose, which we interpret to be correlated with accumulated radiation damage, on He diffusivity. This effect is manifest in both date-effective uranium (eU) correlations among zircon grains from single hand samples and in diffusion experiments on pairs of crystallographically oriented slabs of zircon with alpha doses ranging from ~10^{16} to 10^{19} α/g. We interpret these results as due to two contrasting effects of radiation damage in zircon, both of which have much larger effects on He diffusivity and thermal sensitivity of the zircon (U-Th)/He system than crystallographic anisotropy. Between 1.2×10^{16} α/g and 1.4×10^{18} α/g, the frequency factor, D_0, measured in the c-axis parallel direction decreases by roughly four orders of magnitude, causing He diffusivity to decrease dramatically (for example by three orders of magnitude at temperatures between 140 and 220 °C). Above ~2×10^{18} α/g, however, activation energy decreases by a factor of roughly two, and diffusivity increases by about nine orders of magnitude by 8.2×10^{18} α/g. We interpret these two trends with a model that describes the increasing tortuosity of diffusion pathways with progressive damage accumulation, which in turn causes decreases in He diffusivity at low damage. At high damage, increasing diffusivity results from damage zone interconnection and consequential shrinking of the effective diffusion domain size. Our model predicts that the bulk zircon (U-Th)/He closure temperature (T_c) increases from about 140 to 220 °C between alpha doses of 10^{16} to 10^{18} α/g, followed by a dramatic decrease in T_c above this dose. Linking this parameterization to one describing damage annealing as a function of time and temperature, we can model the coevolution of damage, He diffusivity, and (U-Th)/He date of zircon. This model generates positive or negative date-eU correlations depending on the extent of damage in each grain and the date-eU sample's time-temperature history.

Key words: Zircon, He diffusion, thermochronology, radiation damage

INTRODUCTION

Over the last decade, numerous studies have used zircon (U-Th)/He (zircon He) thermochronology to interpret thermal histories and geologic processes. Accurate and realistic interpretations using this thermochronometer, as well as constraints on convenient indices like closure temperature (T_c) and the partial retention zone (PRZ),

* Department of Geosciences, University of Arizona, 1040 E. 4th Street, Tucson, Arizona 85721 U.S.A.
** Jackson School of Geosciences, University of Texas, Austin, Texas 78712 U.S.A.
*** Institute for Mineralogy and Crystallography, University of Vienna, Althanstrasse 14, 1090, Vienna, Austria
† Corresponding author: wrg@email.arizona.edu; phone: 507-301-8884; fax: 520-621-2672

require quantitative understanding of the kinetics of He diffusion in zircon, including the effects of temperature, crystallographic orientation, and radiation damage. Most zircon He dating studies thus far have assumed that the kinetics measured on a few zircons from a limited number of locations (Reiners and others, 2002; Reiners and others, 2004; Wolfe and Stockli, 2010) apply to all zircons found in a wide range of geologic settings. This assumption may be appropriate, at least to first order, in some cases, as demonstrated by geologically consistent results from settings such as deep drill cores (Wolfe and Stockli, 2010). But several aspects of He diffusion in zircon are likely to be more complicated, which may lead to more complex results in some applications.

Anisotropic He diffusion in zircon is one such complication. Molecular dynamic simulations (Reich and others, 2007; Saadoune and others, 2009; Bengston and others, 2012) and laboratory measurements (Farley, 2007; Cherniak and others, 2009) have demonstrated that He diffusion is faster in the c-axis parallel direction than the c-axis orthogonal direction, at least in specimens with little or no radiation damage or other type of defects. These studies might suggest that grain aspect ratios may influence diffusion kinetics. Watson and others (2010) introduced analytical and numerical methods that allow consideration of the degree to which anisotropy affects both the calculation of bulk He loss from a zircon and step-heating results. However, results from our study suggest that anisotropy is a relatively minor problem for interpreting zircon He dates compared with the effects of radiation damage, which are less well understood.

Damage results from self-irradiation, primarily by recoils of heavy daughter nuclei upon emission of an alpha particle, but also by spontaneous fission events and the alpha particles themselves. Because radiation damage can be annealed at elevated temperatures (for example, Zhang and others, 2000), its extent in a grain can be predicted only roughly by calculating time-integrated self-irradiation doses. These doses can be calculated from the concentration of effective uranium (eU) as scaled for relative alpha production rate ($eU = U + 0.235 \times Th$), and an estimate of the time since the sample was cooled below the threshold temperature for long-term damage annealing. Nasdala and others (2004a) showed that alpha doses calculated using a zircon's U-Pb date may overestimate the radiation damage present, as their Sri Lankan samples experienced annealing post-dating each zircon's U-Pb date. Instead, they calculated "effective alpha doses" by applying a correction factor that accounts for the partial long-term annealing. This correction factor was in part calibrated with Raman spectroscopy, a more direct technique than estimating alpha dose for quantifying damage. Unfortunately, this calibration was specific to Nasdala and other's (2004a) particular suite of zircons, which makes it difficult to broadly use in constraining the threshold temperature of long-term annealing. Furthermore, as we will discuss in greater detail in later sections, there is no consensus on how to model the kinetics of alpha recoil damage on either laboratory or geologic timescales. For samples with simple thermal histories, it may be possible to roughly estimate the duration over which radiation damage has accumulated from the density of spontaneous fission tracks. To the best of our knowledge, the kinetics of fission-track annealing are the only ones available that describe damage annealing of any type in zircon on geologic timescales (for example, Rahn and others, 2004; Tagami, 2005; Yamada and others, 2007), and if the apatite system serves as a comparison (for example, Shuster and Farley, 2009), then it is reasonable to expect that they correlate with the kinetics of alpha recoil damage annealing. Current estimates of the ZFT partial annealing zone (that is, threshold temperature for annealing) are 262 to 330 °C at an isothermal hold-time of 10 my (Yamada and others, 2007), although Garver and others (2005) have shown that annealing temperatures can be as low as 180 °C in heavily damaged

zircons. Again, we leave a more detailed discussion of the limitations of comparing these two types of damage annealing to a later section, but for now assume that ZFT kinetics provide an estimate of the degree of structural annealing in zircon. Thus, as long as zircon He dates are either similar to ZFT dates, or if we can assume from geologic constraints that He dates record a pulse of rapid cooling from temperatures consistent with the ZFT partial annealing zone, then He dates can be used to estimate the duration over which radiation damage has accumulated, and this, combined with effective U concentration, provides an estimate of the "effective alpha dose." In this paper, we report alpha doses following this assumption, unless stated otherwise.

Previous work on He diffusion in zircon focused mostly on differences between specimens from the same rock sample with alpha doses greater or less than $\sim 2 \times 10^{18}$ α/g (Hurley, 1952; Holland, 1954; Hurley and others, 1956; Reiners, 2005). At doses higher than $\sim 2 \times 10^{18}$ α/g, zircon He dates in these studies become systematically younger with increasing damage. Nasdala and others (2004a) proposed this was likely due to the extensive inter-connection of boundaries between crystalline and amorphous domains at moderate degrees of radiation damage, at damage levels beyond the first percolation point as proposed by Salje and others (1999), which opens up a three-dimensional network of pathways for He migration. Subsequent modeling by Ketcham and others (2013) indicated that the important percolating phase may be damage from spontaneous fission, as alpha recoil damage percolation occurs at two orders of magnitude lower alpha dose. Reiners (2005) attempted to match the progressively younger dates with the trend line of decreasing fraction of remaining crystallinity as determined by another percolation-based model that accounts for the double-overlapping of damage cascades (Weber and others, 1994). This approach had only limited success, however, as only one dataset conformed to this model. This suggests a more sophisticated understanding of the damage-diffusivity relationship at high amounts of damage is required.

In contrast to the relatively well documented behavior at high extents of damage in zircon, little attention has been paid to potential damage-diffusivity relationships at low degrees of radiation damage, where the effects on He diffusion may be quite different. In apatite, for example, He diffusivity decreases with increasing damage (Shuster and others, 2006; Flowers and others, 2009; Gautheron and others, 2009; Shuster and Farley, 2009). This has been interpreted as a result of preferential partitioning (that is, "trapping") of He in damage zones, impeding diffusion. This is manifest as positive correlations between apatite He date and (eU), which, among specimens from a sample that experienced a common time-temperature (t-T) history, is a proxy for relative extents of radiation damage.

In this study, we found that zircon He dates from some geologic settings also display positive date-eU correlations, which we interpret to be a result of damage at low alpha doses. We also observe negative date-eU correlations and, in some instances, both types of correlations may be present in a single sample. Throughout this paper, we use the span in eU concentrations for zircons from the same sample as a first-order proxy for each zircon's degree of radiation damage. Although more direct measurements of radiation damage (for example, Raman spectroscopy) would be ideal, for cases where such data are lacking and where zircons share a common thermal history (that is, all zircons experienced any annealing at the same time), date-eU correlations manifest the effect that damage has on He diffusivity. A quantitative explanation of these correlations requires a new, damage-based model for He diffusion in zircon. To develop this model, we conducted a series of step-heating diffusion experiments on zircons with self-irradiation doses spanning nearly three orders of magnitude ($\sim 10^{16}$ to 10^{19} α/g). With the kinetics from these experiments, we parameterize a relationship between alpha dose and radiation damage, and He diffusivity, that accounts for

decreases in diffusivity at low damage and increases in diffusivity at high damage. Finally, similar to the apatite radiation damage accumulation and annealing model (RDAAM, Flowers and others, 2009), we combine this new damage-diffusivity parameterization with a damage annealing model to use various date-eU correlations to constrain candidate *t-T* paths. Our new zircon damage and annealing model both explains zircon He datasets that do not conform to the canonical kinetics of Reiners and others (2004), and allows geologists to use zircon He date-eU correlations to place additional constraints on a sample's *t-T* history.

METHODS

(U-Th)/He Dating

To demonstrate correlations between zircon He date and eU that we interpret as resulting from radiation damage effects on He diffusivity, we show results from samples from both newly reported and previously published zircon He datasets. Zircon He dates from the Sri Lankan dataset were reported previously by Nasdala and others (2004a) while new data include samples from the Miocene Marnoso-Arenacea Formation in the Italian Apennines, sedimentary and basement units associated with the US Cordillera in Utah and Wyoming, and meta-sedimentary rocks from the Cooma Metamorphic Complex in Australia. Our Utah sample resides in the hanging wall of a major Sevier belt thrust sheet (Absaroka). Balanced cross-sections from this location suggest that this sample has undergone kilometer-scale tectonic and sedimentary burial (DeCelles, 1994). The other western US sample is a well sample from La Barge, Wyoming, that was collected in the footwall of the Hogsback thrust at a depth of ~4 km.

We report single-grain zircon He dates, which were analyzed by a number of researchers over the last decade at both Yale University and the University of Arizona. Analytical methods were similar for all samples. Mineral separation followed standard crushing, sieving, and magnetic and density separation procedures. Analysts used methods described by Reiners (2005) that included Nd:YAG and CO_2 laser heating, cryogenic purification, and quadrupole mass spectrometry for ^{4}He analysis, and isotope high-resolution inductively coupled plasma spectrometry for U and Th analysis. Results are reported using the method of Hourigan and others (2005) for the alpha ejection correction.

^{4}He Diffusion Experiments

Sample selection.—For new diffusion experiments we selected samples based on three criteria: 1) the sample was large enough to allow preparation of crystallographically oriented slabs with high aspect ratios (~10), 2) U and Th concentrations were uniform and slabs came from zircon interiors so as to avoid alpha ejection loss or diffusive rounding of He, and 3) the extent of structural radiation damage was characterized by Raman analyses. In addition to characterizing the degree of damage, we also calculate the alpha dose of each sample.

Because we desire samples with both a rapid high temperature to low temperature cooling history, and samples whose radiation damage can be measured by some direct method (Raman, IR spectroscopy, TEM, *et cetera*), we have selected several zircon specimens (RB140, BR231, M127, G3, and N17) from the Sri Lankan dataset of Nasdala and others (2004a). The geo- and thermochronologic characteristics of these zircons, as well as their structural damage, have been well characterized with a number of different techniques. Results suggest that they have all experienced a similar, probably geologically rapid, cooling event at about 420 to 440 Ma. As a check for uniform U and Th distribution in our Sri Lankan zircons, we rely on the backscattered electron and cathodoluminescence images reported by Nasdala and others (2004a),

which demonstrated that all of the zircons from the Sri Lankan suite possess little or no U and Th zonation (images for M127 were not detailed by these authors, but this zircon was subjected to the same analyses and yielded similar results). We also note that the Raman spectra for the Sri Lankan zircons were uniform, further evidence against zonation. We calculated alpha doses using the previously reported zircon He dates for each sample (Nasdala and others, 2004a), except in the case of N17, which—due to the fact that it loses significant amounts of He at room temperature—was calculated using a date consistent with the other Sri Lankan samples (430 Ma). Our calculated doses range from 4.7×10^{17} to 8.2×10^{18} α/g (table 1).

We also measured diffusion properties on a zircon specimen from the Mud Tank carbonatite in Australia, to provide an example with relatively low amounts of damage. We calculate an "effective alpha dose" using an age of 300 Ma, which corresponds to the timing for regional exhumation associated with the Alice Springs orogeny as determined from Rb-Sr dates on biotite and apatite fission track dates (Green and others, 2006). Mud Tank has been used previously in He and Pb diffusion studies (for example, Cherniak and Watson, 2003; Cherniak and others, 2009) and adequately satisfies our other two selection criteria. Uniform U and Th concentration was checked in part through the use of Raman spectroscopy, detailed below.

Sample preparation, Raman spectroscopy.—As a direct quantification of radiation damage, we use the full width at half-maximum (FWHM) of the $\upsilon_3(SiO_4)$ Raman band near the 1000 cm^{-1} Raman shift (for example, Nasdala and others, 2001). This FWHM broadens from initially <2 cm^{-1} for well crystallized to >30 cm^{-1} for severely radiation-damaged zircon (Nasdala and others, 1995). Nasdala and others (2004a) obtained FWHM numbers for the Sri Lankan samples used in our study, and we include these values in table 1.

FWHM numbers for the Mud Tank zircon have not been previously reported and we therefore measured new Raman spectra for this zircon. As a check for possible damage annealing caused by the step-heating experiments, we also measured Raman spectra on pieces of M127 after step-heating and after the final degassing by laser heating. We obtained several Raman spectra at room temperature with a dispersive Horiba Jobin Yvon LabRAM HR 800 spectrometer. This system was equipped with an Olympus BX41 optical microscope, an Olympus 100× objective (n.a. = 0.90), a diffraction grating with 1,800 grooves/mm, and a Si-based, Peltier-cooled charge-coupled device (CCD) detector. Spectra were excited with the He–Ne 632.8 nm emission (3 mW at the sample). We calibrated the spectrometer using the Rayleigh line and neon lamp emissions. The wavenumber accuracy was better than 0.5 cm^{-1}, and the spectral resolution was determined at $\sim$0.8 cm^{-1}. Band fitting was done after appropriate background correction, assuming Lorentzian-Gaussian band shapes. We corrected our measured FWHMs for the experimental band broadening (that is, apparatus function), and real FWHMs were calculated according to the simplified procedure of Dijkman and van der Maas (1976). Total uncertainties of corrected FWHMs are assessed to vary between $\pm$0.4 cm^{-1} (FWHM values smaller than 6 cm^{-1}) and $\pm$1.2 cm^{-1} (FWHM values of $\sim$20 cm^{-1}).

Sample preparation, slab orientation.—To control for crystallographic direction, we oriented each millimeter-scale sample with single-crystal X-ray diffraction analysis. Samples were attached individually to a glass fiber and placed in a Nonius Kappa CCD diffractometer. Ten frames with a step width of 2° were taken with Mo–K_α radiation. We registered several hundred Bragg reflections, which was more than sufficient to determine the sample's crystallographic orientation. A small glass capillary was oriented parallel to the sample's crystallographic [001] direction and then glued onto the specimen. For the grinding and polishing process, we attached our samples to a glass slide, with the glass capillary oriented either parallel or perpendicular to the slide. The

TABLE 1

Zircon slab data

Sample Name	Slab Orientation (relative to c)	Thickness (μm)	U (ppm)	Th (ppm)	(U-Th)/He Date (Ma)	Fluence (x 10^{16} α/g)	FWHM (cm^{-1})	Shift (cm^{-1})
Mud Tank[1,2]	Orthogonal	100	11	5	~300	1.22	2.1±0.2	1008.3±0.1
Mud Tank[1,2]	Parallel	100	11	5	~300	1.22	2.1±0.2	1008.3±0.1
RB140[3]	Orthogonal	40	288	122	437 ± 20	46.7	6.3±0.5	1004.7±0.5
RB140[3]	Parallel	90	288	122	437 ± 20	46.7	6.3±0.5	1004.7±0.5
BR231[3]	Orthogonal	50	772	109	438 ± 20	121	11.0±0.8	1000.6±0.5
M127[3]	Orthogonal	90	923	439	427 ± 20	148	13.6±1.0	1000.2±0.5
M127[3]	Parallel	150	923	439	427 ± 20	148	13.6±1.0	1000.2±0.5
G3[3]	Orthogonal	67	2572	585	441 ± 21	404	30.4±2.5	996.2±0.5
N17[3]	n.a.	150	5568	344	99.2 ± 4.6	821	n.a.	n.a.

Notes: Fluence calculated using reported (U-Th)/He date, except for N17, which was assigned a representative date consistent with other Sri Lankan samples (430 Ma).

[1] U and Th concentrations from Cherniak and others (2009).

[2] (U-Th)/He estimated from biotite Rb-Sr and apatite fission track dates (Green and others, 2006).

[3] Sri Lankan zircon. (U-Th)/He date, FWHM, and shift have been previously reported in Nasdala and others (2004a).

attachment was done with an acetone-soluble glue that hardens, and can be dissolved, at room temperature (UHU hart). After the top polished side was finished, we detached our samples from the glass slide, turned them over, and attached them again, to produce plane-parallel, doubly polished slabs. Temperatures never rose above ~40 °C throughout the entire preparation process. The slab thicknesses (in the range of 40-110 μm) were chosen, depending on slab sizes, to get aspect ratios of 10:1 or higher. This process produced two oriented slabs per sample, one in the c-axis parallel direction (PAR_C), the other c-axis orthogonal (ORT_C).

Step-heating experiments.—We conducted our diffusion experiments on a He extraction/measurement line at the University of Arizona and used the cycled, step-heating procedure and projector-bulb furnace setup of Farley and others (1999). Slabs were held isothermally for durations between 10 and 1590 minutes, and the gas released by each step was cryogenically purified and analyzed for ^{4}He with a quadrupole mass spectrometer. In general, we maintained a similar time-temperature schedule for all slabs: an initial low temperature step at 150 °C, followed by a prograde series of steps in 10 degree increments to 500 °C, followed by a retrograde series of steps to 265 °C, and a final prograde cycle back up to 500 °C. Due to differences in slab size, and in order to release more than just a few percent of gas, some deviations in the length of certain temperature steps were necessary. Time-steps on the initial retrograde cycle often varied and some slabs required additional cycling between 400 and 500 °C. The schedules for samples G3 and N17 involved lower maximum temperatures (383 °C and 270 °C, respectively) and several short time steps (10-30 minutes) because of their high diffusivities. After the step-heating extractions, we completely degassed each sample by laser heating to measure the remaining fraction. A significant fraction of gas was accidentally pumped away and lost during the final degassing of one sample, M127_PAR_C. As such, we calculate the total amount of gas for this sample using the measured U and Th concentration, the zircon He date, and our measured slab dimensions. The same calculation from nearly all of our other samples agrees with observed releases within a few percent. We include this sample in all subsequent tables and figures.

RESULTS

Zircon He Dates: Positive and Negative Date-eU Correlations

We report zircon He dates for all previously unpublished samples in table 2. These data are plotted in figures 1 and 2 and show positive, negative, and sometimes both types of correlations between date and eU in the same sample between date and eU. Each correlation (except for Cooma) represents a collection of single grain dates from a single igneous or sedimentary sample. Importantly, all of the grains in a given correlation have experienced the same *t-T* history for igneous samples, and the same post-depositional *t-T* history for sedimentary samples.

A comparison between figures 1 and 2 highlights several features of both types of correlations. In figure 1, the correlations are generally positive and show an increase in date with eU. In all samples the oldest dates in each one span a range from roughly 30 Ma to as great as 300 Ma, while eU concentrations are as low as ~100 ppm, but no greater than ~1500 ppm. In contrast, samples with negative date-eU correlations (fig. 2) tend to have older maximum dates and higher eU concentrations. These correlations include new results from the Archean basement exposed in the Bighorn Mountains, Wyoming and the Minnesota River valley, Minnesota, and placer zircons from Sri Lanka (Nasdala and others, 2004a). The oldest dates in each of these samples range from approximately 300 Ma to nearly 1.0 Ga and are almost all significantly older than any dates shown in figure 1. Although concentrations of eU overlap somewhat with samples shown in figure 1, the highest concentrations in the Minnesota, Sri

Table 2

Zircon (U-Th)/He data

Sample Name	Sample Location	Rock Type	Mass (μg)	Halfwidth (μm)	U (ppm)	Th (ppm)	^{4}He (nmol/g)	Ft	Corr. Age (Ma)	Analyt. ± (2σ)
04EQ1zA	Minnesota River Valley	Igneous	4.49	41	781	203	1156	0.75	336	14
04EQ1zB	Minnesota River Valley	Igneous	5.96	42	748	218	987	0.77	292	16
04EQ1zC	Minnesota River Valley	Igneous	4.58	36	894	246	294	0.74	76.5	2.9
04EQ1zD	Minnesota River Valley	Igneous	2.55	31	866	166	144	0.70	42.0	2.4
04EQ1zE	Minnesota River Valley	Igneous	3.87	35	1107	351	270	0.73	57.4	2.9
04EQ1zF	Minnesota River Valley	Igneous	9.55	43	647	284	946	0.78	307	12
04GF1zA	Minnesota River Valley	Igneous	10.7	56	247	88.4	948	0.82	758	45
04GF1zB	Minnesota River Valley	Igneous	21.9	63	254	104	1023	0.84	760	30
04MT1zA	Minnesota River Valley	Igneous	26.0	67	362	88.8	1183	0.85	638	102
04MT1zB	Minnesota River Valley	Igneous	31.6	68	346	78.0	1012	0.86	574	92
04R1zA	Minnesota River Valley	Igneous	5.96	42	656	167	1383	0.77	464	18
04R1zB	Minnesota River Valley	Igneous	10.2	51	580	174	1750	0.81	619	25
04RF1zA	Minnesota River Valley	Igneous	16.1	64	84.0	67.3	443	0.83	925	148
04RF1zB	Minnesota River Valley	Igneous	28.8	72	155	177	619	0.86	650	104
04SC1zA	Minnesota River Valley	Igneous	4.82	47	422	110	1663	0.77	843	135
04SC1zB	Minnesota River Valley	Igneous	25.0	71	415	111	1667	0.86	769	123
04SG1zB	Minnesota River Valley	Igneous	9.72	55	1738	1171	790	0.81	89.2	3.9
04SH1zA	Minnesota River Valley	Igneous	10.5	50	1011	228	65.6	0.81	14.2	0.57
04SH1zB	Minnesota River Valley	Igneous	17.2	56	883	184	1144	0.83	271	11
AP9B39	Italian Apennines	Detrital	3.37	37	231	59.0	17.0	0.79	12.2	0.57
AP9B69	Italian Apennines	Detrital	7.89	53	397	188	10.4	0.84	19.2	0.88
AP9B112	Italian Apennines	Detrital	1.99	36	783	197	27.0	0.78	17.8	0.84
AP9B124	Italian Apennines	Detrital	5.96	49	232	77.3	61.8	0.83	9.22	0.44
AP9B136	Italian Apennines	Detrital	4.57	36	450	237	12.8	0.80	12.4	0.57
AP9B147	Italian Apennines	Detrital	6.97	51	259	111	33.6	0.84	13.1	0.60
AP9B186	Italian Apennines	Detrital	2.41	39	321	150	27.0	0.79	17.7	0.84
AP9B187	Italian Apennines	Detrital	2.63	33	426	38.4	38.5	0.78	18.4	0.90

Table 2
(continued)

Sample Name	Sample Location	Rock Type	Mass (μg)	Halfwidth (μm)	U (ppm)	Th (ppm)	^{4}He (nmol/g)	Ft	Corr. Age (Ma)	Analyt. ± (2σ)
AP54B44	Italian Apennines	Detrital	4.11	51	185	80.6	10.2	0.83	11.2	0.45
AP54B55	Italian Apennines	Detrital	2.84	33	934	304	76.2	0.77	18.3	0.75
AP54B64	Italian Apennines	Detrital	3.01	38	585	203	58.2	0.78	21.8	0.84
AP54B65	Italian Apennines	Detrital	3.64	50	746	49.4	58.2	0.82	17.4	0.73
AP54B95	Italian Apennines	Detrital	4.49	59	259	72.1	18.7	0.83	15.1	0.59
AP54B122	Italian Apennines	Detrital	4.58	51	296	95.4	23.6	0.82	16.7	0.64
AP54B127	Italian Apennines	Detrital	14.8	61	501	204	44.6	0.87	17.4	0.67
AP54B129	Italian Apennines	Detrital	2.93	41	124	68.1	8.96	0.80	14.8	0.57
ANU03-055-04	Cooma, Australia	Metasedimentary	6.79	67	313	101	498	0.82	326	15
ANU03-055-07	Cooma, Australia	Metasedimentary	13.4	75	92.3	64.8	153	0.85	303	13
ANU03-055-14	Cooma, Australia	Metasedimentary	14.8	85	455	132	747	0.86	323	14
ANU03-055-22	Cooma, Australia	Metasedimentary	6.80	67	131	52.8	190	0.82	294	13
ANU03-055-26	Cooma, Australia	Metasedimentary	10.54	72	654	436	1213	0.84	345	14
ANU03-056-05	Cooma, Australia	Metasedimentary	1.53	31	844	83.8	1059	0.68	329	14
ANU03-056-09	Cooma, Australia	Metasedimentary	3.31	43	1229	321	1276	0.76	235	10
ANU03-056-13	Cooma, Australia	Metasedimentary	3.49	32	576	188	822	0.72	336	14
ANU03-056-16	Cooma, Australia	Metasedimentary	4.17	41	996	167	1111	0.76	259	11
ANU03-056-22	Cooma, Australia	Metasedimentary	6.97	46	1097	391	1227	0.78	240	10
BH12zA	Bighorns, Wyoming	Igneous	8.22	56	1552	416	227	0.80	31.7	0.49
BH12zB	Bighorns, Wyoming	Igneous	46.4	88	1736	328	57.1	0.88	6.60	0.27
BH12zC	Bighorns, Wyoming	Igneous	32.6	74	876	214	779	0.87	178	7.2
BH12zD	Bighorns, Wyoming	Igneous	8.41	50	1275	278	165	0.80	28.5	1.1
BH12zE	Bighorns, Wyoming	Igneous	4.91	43	1169	372	90.1	0.76	17.4	0.68
BH12zM	Bighorns, Wyoming	Igneous	4.93	42	1589	329	95.5	0.76	14.0	0.56
BH12zN	Bighorns, Wyoming	Igneous	5.41	42	1166	324	107	0.77	20.8	0.81
BH17zA	Bighorns, Wyoming	Igneous	10.2	52	300	108	805	0.82	542	8.9
BH17zB	Bighorns, Wyoming	Igneous	15.0	60	414	255	714	0.83	329	14

Table 2
(continued)

Sample Name	Sample Location	Rock Type	Mass (μg)	Halfwidth (μm)	U (ppm)	Th (ppm)	^{4}He (nmol/g)	Ft	Corr. Age (Ma)	Analyt. ± (2σ)
BH17zC	Bighorns, Wyoming	Igneous	4.34	39	426	219	1023	0.75	513	22
BH17zD	Bighorns, Wyoming	Igneous	1.73	30	439	334	655	0.67	343	14
BH17zE	Bighorns, Wyoming	Igneous	3.32	37	367	219	966	0.73	569	24
EM12907zA	La Barge, Wyoming	Detrital	6.58	51	285	134	286	0.80	207	8.6
EM12907zB	La Barge, Wyoming	Detrital	6.69	59	101	62.2	29.2	0.81	57.3	2.6
EM12907zC	La Barge, Wyoming	Detrital	5.33	51	70.9	78.1	10.6	0.79	27.9	1.2
EM13270zA	La Barge, Wyoming	Detrital	4.68	48	232	145	179	0.78	158	7.5
EM13270zB	La Barge, Wyoming	Detrital	3.60	45	134	81.5	44.9	0.76	70.7	3.3
EM13270zC	La Barge, Wyoming	Detrital	4.72	51	662	244	635	0.79	204	9.8
EM13105zA	La Barge, Wyoming	Detrital	2.60	41	199	137	90.2	0.74	96.9	4.4
EM13105zB	La Barge, Wyoming	Detrital	3.30	42	292	176	210	0.75	153	7.2
EM13105zC	La Barge, Wyoming	Detrital	4.54	45	258	110	255	0.77	213	10
Z-AV-K2-8	Kelvin Formation, Utah	Detrital	3.14	38	198	70.3	80.9	0.79	87.8	3.9
Z-AV-K2-18	Kelvin Formation, Utah	Detrital	1.31	25	217	86	87.3	0.71	95.4	4.4
Z-AV-K2-20	Kelvin Formation, Utah	Detrital	4.47	39	265	57.7	127	0.80	105	5.0
Z-AV-K2-40	Kelvin Formation, Utah	Detrital	1.23	31	339	117	437	0.73	244	14
Z-AV-K2-52	Kelvin Formation, Utah	Detrital	0.443	21	1421	134	1585	0.64	309	20
Z-AV-K2-95	Kelvin Formation, Utah	Detrital	2.37	38	483	113	695	0.79	268	15

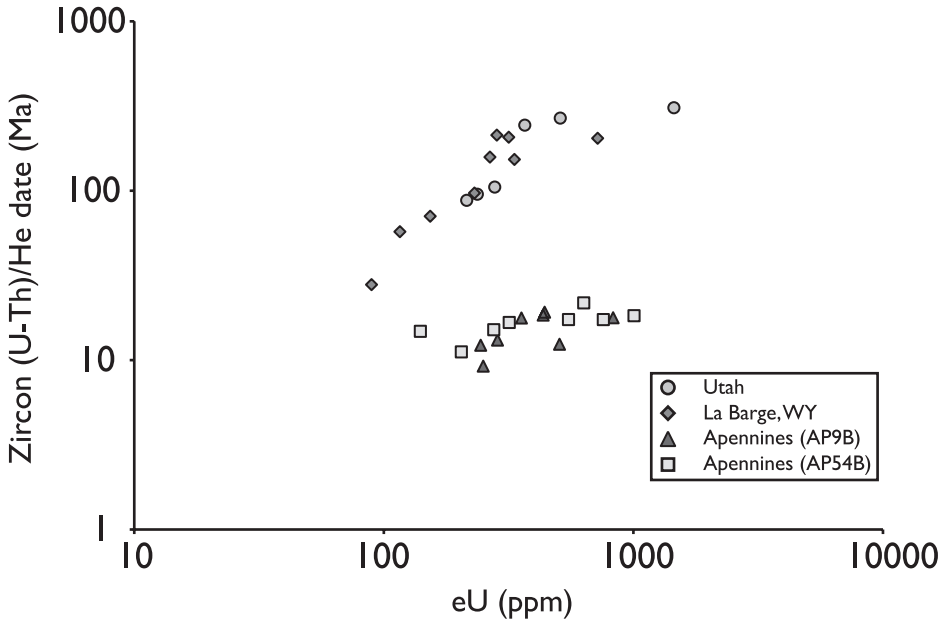

Fig. 1. Positive date-eU correlations. Individual points in each dataset represent single grain dates (2 sigma error).

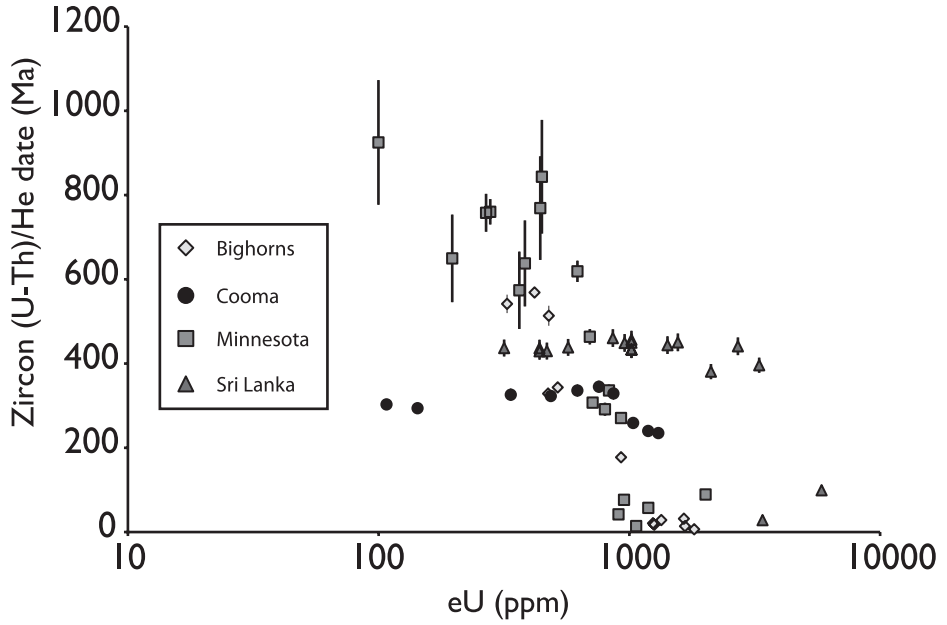

Fig. 2. Negative date-eU correlations. Individual points in each dataset represent single grain ages (2 sigma error).

Lankan and Big Horns samples are all greater than 2000 ppm, and a few Sri Lankan grains are greater than 4000 ppm. We also observe differences in the shape of the negative correlation for each sample: some are broadly continuously negative (for example Minnesota, Bighorns), whereas others appear to have a date plateau followed by a steep decline at high damage amounts (for example Sri Lanka). The rollover from reproducible dates to negative trends begins at different eU concentrations in each sample, which further suggests that each correlation has a unique form. Similar to the Sri Lankan grains, a composite sample, Cooma, shows a drop off in dates at a threshold eU; however, instead of a date plateau this appears to have a slight positive correlation at lower eU concentrations. Thus, we observe positive, negative, and sometimes both types of date-eU correlations in certain samples. In general, negative correlations occur in samples with old maximum dates (100-1000 Ma) and high eU concentrations (>2000 ppm), and positive correlations occur in samples with young maximum dates (10-100 Ma) and low eU concentrations (10-1500 ppm).

Raman Spectroscopy

The Mud Tank zircon yielded measured Raman FWHMs in the range of 2.0 to 2.3 cm^{-1}. These FWHMs refer to the main SiO_4 stretching band, which was observed at 1008.2 to 1008.4 cm^{-1}. After mathematical correction for the artificial band broadening due to the spectrometer's limited spectral resolution, we transformed the measured FWHM values to real FWHMs of 1.7 to 2.0 cm^{-1}. Both parameters are indistinguishable from Raman values of synthetic $ZrSiO_4$ of 1008.3 cm^{-1} Raman shift and 1.8 cm^{-1} FWHM (Nasdala and others, 2002). Consequently, the Mud Tank material represents an extremely low degree of radiation damage, which is close to, or even below, the detection sensitivity of the Raman technique. Mud Tank's low damage is further supported by a low calculated alpha dose of 1.2×10^{16} α/g and a broad-band yellow cathodoluminescence (Nasdala and others, 2004b), which is only observed at extremely low defect densities (Nasdala and others, 2011).

After step-heating, the FWHM for M127 was 11.2 to 13.2 cm^{-1} observed at 1001.5 to 1002.5 cm^{-1}. Compared to the published results for unannealed M127 (13.7-14.7 cm^{-1} at 999-1000 cm^{-1}), these values represent a minor degree of annealing and suggest that our standard heating schedule is not substantially annealing the amount of damage in our samples. Following final laser heating, the FWHMs were lowered to ~2.0 cm^{-1} at ~1008 cm^{-1}, which is close to the values for synthetic, undamaged zircon.

Diffusion Experiments

Results of step-heating experiments are shown in table 3 and as Arrhenius trends in figure 3. For the Arrhenius trends, we use the fractional gas loss equation for a plane sheet geometry to calculate D/a^2 values at each temperature step (Fechtig and Kalbitzer, 1966). A striking feature in all of these plots is the non-linear behavior of diffusivities in the initial prograde temperature steps. Other studies have observed such behavior as well (Reiners and others, 2002; Reiners and others, 2004) and this non-linearity often manifests as a convex-up curve. In RB140, BR231, and M127, the curve is positioned above the linear Arrhenius trend, whereas in Mud Tank, G3, and N17 the curve is positioned below the linear Arrhenius trend. As temperature increased, however, the trend became linear after the first tenths to couple of percent of gas was released in nearly all samples (except for N17). This is apparent in a plot of $\ln(a/a_0)$ as a function of cumulative gas released (fig. 4). Furthermore, as was observed in previous studies (Reiners and others, 2002; Reiners and others, 2004), this behavior seemed to disappear after the highest temperatures were reached in the initial prograde path and was almost completely absent in all subsequent steps (fig. 4, see table 3 for corresponding fraction degassed). Interestingly though, a subtle return to

TABLE 3

Step heating results

Step	T °C	seconds	^{4}He (pmol)	$f_{cumulative}$	$\ln(D/a^2)^1$
		Mud Tank Orthogonal			
1	150	3600	0.0013	0.000067	-27.66
2	160	7200	0.0014	0.000134	-27.23
3	170	7200	0.0240	0.001323	-22.39
4	180	7200	0.0155	0.002090	-21.98
5	190	7200	0.0059	0.002380	-22.68
6	200	7200	0.0024	0.002500	-23.48
7	210	7200	0.0024	0.002618	-23.44
8	220	7200	0.0007	0.002654	-24.59
9	230	7200	0.0025	0.002777	-23.34
10	240	7200	0.0022	0.002888	-23.41
11	250	7200	0.0025	0.003012	-23.25
12	260	7200	0.0028	0.003151	-23.09
13	270	7200	0.0045	0.003376	-22.56
14	280	7200	0.0073	0.003736	-22.00
15	290	7200	0.0114	0.004300	-21.43
16	300	7200	0.0174	0.005164	-20.84
17	310	5400	0.0184	0.006078	-20.32
18	320	5400	0.0314	0.007637	-19.59
19	330	5400	0.0484	0.010040	-18.90
20	340	3600	0.0454	0.012291	-18.33
21	350	3600	0.0636	0.015446	-17.77
22	360	3600	0.0892	0.019871	-17.19
23	370	3600	0.1175	0.025701	-16.66
24	380	3600	0.1806	0.034663	-15.95
25	390	3600	0.2168	0.045420	-15.49
26	400	3600	0.3518	0.062878	-14.70
27	410	3600	0.4659	0.085997	-14.10
28	420	1800	0.2617	0.098980	-13.77
29	430	1800	0.3459	0.116143	-13.34
30	440	1800	0.4907	0.140492	-12.81
31	450	1800	0.5884	0.169688	-12.44
32	460	1800	0.6934	0.204092	-12.09
33	470	1800	0.8256	0.245054	-11.73
34	480	1800	1.0619	0.297746	-11.29
35	490	1800	1.2457	0.359556	-10.94
36	500	1800	1.4048	0.429261	-10.64
37	500	1800	1.2039	0.488995	-10.64
38	495	1800	0.8731	0.532317	-10.86
39	485	1800	0.5510	0.559656	-11.25
40	475	1800	0.3589	0.577466	-11.64
41	465	1800	0.2437	0.589560	-12.00
42	455	1800	0.1600	0.597497	-12.40
43	445	1800	0.1120	0.603054	-12.75
44	435	1800	0.0731	0.606683	-13.17
45	425	1800	0.0471	0.609019	-13.60
46	415	1800	0.0298	0.610498	-14.06
47	405	1800	0.0198	0.611479	-14.46
48	395	3600	0.0254	0.612738	-14.91
49	385	3600	0.0153	0.613496	-15.41
50	375	3600	0.0101	0.613998	-15.82
51	365	5400	0.0075	0.614370	-16.53
52	355	7200	0.0065	0.614694	-16.95
53	345	7200	0.0032	0.614854	-17.66
54	335	14400	0.0042	0.615060	-18.10
55	325	21600	0.0046	0.615290	-18.39
56	315	43200	0.0043	0.615506	-19.15
57	305	43200	0.0024	0.615626	-19.73
58	295	43200	0.0015	0.615702	-20.19
59	285	86400	0.0018	0.615790	-20.74
60	275	86400	0.0010	0.615841	-21.29
61	265	86400	0.0008	0.615881	-21.53
62	273	86400	0.0010	0.615928	-21.35
63	283	86400	0.0017	0.616015	-20.75
64	293	86400	0.0029	0.616157	-20.26

TABLE 3
(continued)

Step	T °C	seconds	^{4}He (pmol)	$f_{cumulative}$	$\ln(D/a^2)^1$
			Mud Tank Orthogonal		
65	303	43200	0.0014	0.616227	-20.27
66	313	43200	0.0029	0.616370	-19.55
67	323	21600	0.0026	0.616500	-18.96
68	343	14400	0.0060	0.616796	-17.73
69	353	7200	0.0048	0.617033	-17.26
70	363	7200	0.0102	0.617537	-16.51
71	373	7200	0.0149	0.618274	-16.12
72	383	7200	0.0235	0.619440	-15.66
73	393	7200	0.0420	0.621525	-15.08
74	403	7200	0.0723	0.625110	-14.53
75	413	7200	0.1189	0.631009	-14.03
76	423	7200	0.1520	0.638550	-13.77
77	433	7200	0.2227	0.649601	-13.38
78	443	3600	0.1597	0.657526	-13.00
79	453	3600	0.2363	0.669252	-12.59
80	463	3600	0.3581	0.687019	-12.16
81	473	3600	0.4370	0.708702	-11.93
82	483	3600	0.5890	0.737928	-11.59
83	493	3600	0.7832	0.776789	-11.26
84	500	3600	0.8300	0.817972	-11.15
Final			3.6682	1	
Total			20.1534		
			Mud Tank Parallel		
1	150	3600	0.0016	0.000063	-27.77
2	160	7200	0.0012	0.000111	-27.73
3	170	7200	0.0010	0.000150	-27.54
4	180	7200	0.0016	0.000211	-26.76
5	190	7200	0.0011	0.000252	-26.90
6	200	7200	0.0012	0.000299	-26.59
7	210	7200	0.0013	0.000350	-26.34
8	220	8100	0.0018	0.000421	-25.96
9	230	7200	0.0018	0.000491	-25.69
10	240	7200	0.0021	0.000572	-25.40
11	250	7200	0.0025	0.000668	-25.06
12	260	7200	0.0030	0.000786	-24.70
13	270	7200	0.0036	0.000927	-24.36
14	280	7200	0.0043	0.001096	-24.01
15	290	7200	0.0054	0.001305	-23.63
16	300	7200	0.0063	0.001552	-23.29
17	310	5400	0.0059	0.001781	-22.92
18	320	5400	0.0072	0.002061	-22.58
19	330	5400	0.0091	0.002416	-22.19
20	340	3600	0.0078	0.002721	-21.80
21	350	3600	0.0106	0.003136	-21.36
22	360	3600	0.0139	0.003682	-20.93
23	370	3600	0.0191	0.004427	-20.45
24	380	3600	0.0253	0.005418	-19.97
25	390	3600	0.0357	0.006815	-19.41
26	400	3600	0.0512	0.008817	-18.80
27	410	3600	0.0706	0.011579	-18.21
28	420	1800	0.0496	0.013518	-17.67
29	430	1800	0.0721	0.016337	-17.12
30	440	1800	0.0993	0.020222	-16.60
31	450	1800	0.1324	0.025401	-16.09
32	460	1800	0.1664	0.031909	-15.63
33	470	1800	0.2080	0.040043	-15.18
34	480	1800	0.2440	0.049585	-14.80
35	490	1800	0.2775	0.060436	-14.47
36	500	1800	0.3234	0.073084	-14.12
37	500	1800	0.2527	0.082966	-14.21
38	495	1800	0.1819	0.090079	-14.44
39	485	1800	0.1195	0.094754	-14.79

TABLE 3
(continued)

Step	T °C	seconds	^{4}He (pmol)	$f_{cumulative}$	$\ln(D/a^2)^1$
			Mud Tank Parallel		
40	475	1800	0.0790	0.097842	-15.16
41	465	1800	0.0563	0.100044	-15.48
42	455	1800	0.0461	0.101846	-15.66
43	445	1800	0.0317	0.103087	-16.01
44	435	1800	0.0218	0.103939	-16.38
45	425	1800	0.0147	0.104514	-16.77
46	415	1800	0.0101	0.104909	-17.14
47	405	1800	0.0069	0.105179	-17.51
48	395	3600	0.0093	0.105544	-17.90
49	385	3600	0.0064	0.105795	-18.28
50	375	3600	0.0041	0.105954	-18.73
51	365	5400	0.0042	0.106119	-19.10
52	355	7200	0.0036	0.106259	-19.55
53	345	7200	0.0024	0.106351	-19.96
54	335	14400	0.0030	0.106468	-20.42
55	325	21600	0.0033	0.106597	-20.72
56	315	43200	0.0038	0.106745	-21.28
57	305	43200	0.0024	0.106840	-21.72
58	295	43200	0.0015	0.106899	-22.20
59	285	92700	0.0023	0.106987	-22.56
60	275	86400	0.0013	0.107039	-23.02
61	265	86400	0.0012	0.107085	-23.12
62	273	86400	0.0016	0.107146	-22.86
63	283	86400	0.0019	0.107219	-22.67
64	293	86400	0.0028	0.107329	-22.26
65	303	43200	0.0015	0.107390	-22.17
66	313	43200	0.0024	0.107485	-21.71
67	323	21600	0.0021	0.107566	-21.18
68	333	14400	0.0008	0.107596	-21.77
69	343	7200	0.0033	0.107726	-19.61
70	353	7200	0.0020	0.107805	-20.10
71	363	7200	0.0040	0.107961	-19.42
72	373	7200	0.0063	0.108206	-18.97
73	383	7200	0.0092	0.108564	-18.59
74	393	7200	0.0146	0.109136	-18.12
75	403	7200	0.0217	0.109984	-17.71
76	413	7200	0.0308	0.111189	-17.35
77	423	7200	0.0441	0.112915	-16.98
78	433	7200	0.0626	0.115363	-16.61
79	443	3600	0.0425	0.117026	-16.29
80	453	3600	0.0596	0.119356	-15.93
81	463	3600	0.0796	0.122469	-15.62
82	473	3600	0.1064	0.126631	-15.30
83	483	3600	0.1378	0.132021	-15.01
84	493	3600	0.1277	0.137013	-15.04
85	500	3600	0.2035	0.144971	-14.53
Final			21.8625	1	
Total			25.5693		
			RB140 Orthogonal		
1	150	7200	0.0165	0.000228	-25.90
2	170	7200	0.0104	0.000371	-25.39
3	180	7200	0.0041	0.000428	-26.03
4	190	7200	0.0036	0.000477	-26.05
5	200	7200	0.0034	0.000524	-26.00
6	210	7200	0.0034	0.000570	-25.92
7	220	7200	0.0033	0.000616	-25.86
8	230	7200	0.0038	0.000668	-25.64
9	240	7200	0.0037	0.000719	-25.58
10	250	7200	0.0042	0.000778	-25.37
11	260	7200	0.0058	0.000858	-24.97
12	270	7200	0.0062	0.000944	-24.81
13	280	7200	0.0071	0.001041	-24.58

TABLE 3
(continued)

Step	T °C	seconds	^{4}He (pmol)	$f_{cumulative}$	$\ln(D/a^2)^1$
		RB140 Orthogonal			
14	290	7200	0.0092	0.001168	-24.21
15	300	7200	0.0126	0.001341	-23.77
16	310	7200	0.0166	0.001569	-23.35
17	320	7200	0.0198	0.001841	-23.01
18	330	7200	0.0284	0.002232	-22.47
19	340	7200	0.0362	0.002730	-22.03
20	350	7200	0.0468	0.003375	-21.57
21	360	7200	0.0596	0.004197	-21.11
22	370	7200	0.0770	0.005257	-20.63
23	380	7200	0.1005	0.006641	-20.14
24	390	7200	0.1262	0.008379	-19.68
25	400	7200	0.1624	0.010616	-19.19
26	410	3600	0.1086	0.012112	-18.72
27	420	3600	0.1447	0.014105	-18.29
28	430	3600	0.1931	0.016764	-17.84
29	440	3600	0.2472	0.020170	-17.41
30	450	3600	0.3114	0.024459	-16.99
31	460	3600	0.3828	0.029732	-16.59
32	470	3720	0.4810	0.036358	-16.20
33	480	3600	0.5621	0.044102	-15.81
34	490	3600	0.7241	0.054076	-15.36
35	500	3600	0.7958	0.065039	-15.07
36	495	3600	0.5659	0.072835	-15.27
37	485	3600	0.3558	0.077736	-15.64
38	475	3600	0.2340	0.080959	-16.01
39	465	3600	0.1554	0.083100	-16.38
40	455	3600	0.0972	0.084440	-16.83
41	445	3600	0.0638	0.085318	-17.24
42	435	3600	0.0414	0.085889	-17.66
43	425	3600	0.0261	0.086248	-18.12
44	415	7200	0.0328	0.086701	-18.58
45	405	7200	0.0226	0.087012	-18.95
46	395	7200	0.0127	0.087187	-19.52
47	385	7200	0.0091	0.087312	-19.85
48	375	7200	0.0054	0.087387	-20.37
49	365	7200	0.0030	0.087429	-20.96
50	355	14400	0.0037	0.087480	-21.45
51	345	14400	0.0020	0.087506	-22.08
52	335	14400	0.0013	0.087524	-22.49
53	325	21600	0.0012	0.087541	-22.97
54	315	21600	0.0007	0.087551	-23.45
55	305	43260	0.0009	0.087563	-24.00
56	295	43200	0.0006	0.087571	-24.44
57	285	50400	0.0006	0.087578	-24.59
58	275	86400	0.0006	0.087587	-25.06
59	265	86400	0.0004	0.087592	-25.42
60	273	82800	0.0003	0.087596	-25.78
61	283	86400	0.0006	0.087604	-25.10
62	293	50400	0.0005	0.087611	-24.62
63	303	54000	0.0006	0.087619	-24.63
64	313	43200	0.0010	0.087634	-23.81
65	323	28800	0.0011	0.087649	-23.33
66	333	28800	0.0018	0.087673	-22.87
67	343	21600	0.0021	0.087703	-22.40
68	353	14400	0.0037	0.087754	-21.43
69	363	14400	0.0049	0.087821	-21.17
70	373	14400	0.0095	0.087953	-20.49
71	383	7200	0.0073	0.088054	-20.06
72	393	7200	0.0117	0.088215	-19.59
73	403	7200	0.0196	0.088485	-19.07
74	413	7200	0.0324	0.088931	-18.57
75	423	7200	0.0474	0.089585	-18.18
76	433	7200	0.0787	0.090669	-17.66
77	443	7200	0.1188	0.092306	-17.24

TABLE 3
(continued)

Step	T °C	seconds	^{4}He (pmol)	$f_{cumulative}$	$\ln(D/a^2)^1$
			RB140 Orthogonal		
78	453	7200	0.1752	0.094719	-16.83
79	463	7200	0.2569	0.098258	-16.41
80	473	7200	0.3596	0.103212	-16.03
81	483	3600	0.2571	0.106754	-15.63
82	493	3600	0.3521	0.111604	-15.28
83	500	3600	0.4319	0.117555	-15.03
Final			64.0589	1	
Total			72.5924		
			RB140 Parallel		
1	150	7200	0.0338	0.000084	-27.89
2	160	7200	0.0082	0.000105	-28.49
3	170	7200	0.0066	0.000121	-28.54
4	180	7200	0.0058	0.000136	-28.54
5	190	7200	0.0048	0.000148	-28.63
6	200	7200	0.0047	0.000159	-28.56
7	210	7200	0.0049	0.000172	-28.45
8	220	7200	0.0051	0.000184	-28.34
9	230	7200	0.0062	0.000200	-28.07
10	240	7200	0.0058	0.000214	-28.05
11	250	7200	0.0076	0.000233	-27.71
12	260	7200	0.0086	0.000254	-27.50
13	270	7200	0.0106	0.000281	-27.20
14	280	7200	0.0135	0.000315	-26.84
15	290	7200	0.0174	0.000358	-26.47
16	300	7200	0.0227	0.000415	-26.07
17	310	5400	0.0228	0.000472	-25.64
18	320	5400	0.0306	0.000548	-25.20
19	330	5400	0.0391	0.000646	-24.80
20	340	3600	0.0346	0.000732	-24.38
21	350	3600	0.0461	0.000847	-23.95
22	360	3600	0.0590	0.000994	-23.55
23	370	3600	0.0731	0.001176	-23.17
24	380	3600	0.0906	0.001402	-22.79
25	390	3600	0.1128	0.001684	-22.39
26	400	3600	0.1382	0.002028	-22.00
27	410	3600	0.1600	0.002427	-21.67
28	420	3600	0.1966	0.002918	-21.28
29	430	3600	0.2383	0.003512	-20.91
30	440	3600	0.2806	0.004212	-20.56
31	450	3600	0.3395	0.005059	-20.19
32	460	3600	0.4008	0.006058	-19.84
33	470	3600	0.4694	0.007229	-19.50
34	480	3600	0.5581	0.008621	-19.15
35	490	1800	0.3411	0.009472	-18.82
36	500	1800	0.4238	0.010529	-18.50
37	500	1800	0.3788	0.011474	-18.52
38	495	1800	0.2849	0.012184	-18.73
39	485	3600	0.3603	0.013083	-19.12
40	475	2760	0.1820	0.013537	-19.49
41	465	3600	0.1521	0.013916	-19.90
42	455	3600	0.0969	0.014158	-20.33
43	445	3600	0.0617	0.014312	-20.77
44	435	3600	0.0400	0.014411	-21.19
45	425	3600	0.0257	0.014475	-21.63
46	415	3600	0.0162	0.014516	-22.09
47	405	3600	0.0101	0.014541	-22.56
48	395	3600	0.0061	0.014556	-23.06
49	385	3600	0.0038	0.014565	-23.54
50	375	3600	0.0023	0.014571	-24.03
51	365	7200	0.0028	0.014578	-24.54
52	355	7200	0.0016	0.014582	-25.08
53	345	7200	0.0010	0.014585	-25.59

TABLE 3
(continued)

Step	T °C	seconds	^{4}He (pmol)	$f_{cumulative}$	$\ln(D/a^2)^1$
			RB140 Parallel		
54	335	14400	0.0016	0.014589	-25.78
55	325	21600	0.0010	0.014591	-26.69
56	315	43200	0.0012	0.014594	-27.18
57	305	43200	0.0008	0.014596	-27.62
58	295	52200	0.0006	0.014597	-28.01
59	285	93600	0.0008	0.014599	-28.36
60	275	86400	0.0006	0.014601	-28.60
61	265	95400	0.0005	0.014602	-28.87
62	273	86400	0.0031	0.014610	-26.92
63	283	86400	0.0015	0.014613	-27.65
64	293	86400	0.0015	0.014617	-27.66
65	303	54000	0.0009	0.014619	-27.70
66	313	54000	0.0013	0.014623	-27.28
67	323	21600	0.0008	0.014625	-26.84
68	324	25200	0.0014	0.014628	-26.45
69	343	21600	0.0008	0.014630	-25.85
70	353	7200	0.0013	0.014634	-25.26
71	363	7200	0.0023	0.014639	-24.71
72	373	7200	0.0039	0.014649	-24.20
73	383	7200	0.0066	0.014665	-23.67
74	393	7200	0.0112	0.014694	-23.13
75	403	7200	0.0182	0.014739	-22.65
76	413	7200	0.0289	0.014811	-22.18
77	423	7200	0.0459	0.014926	-21.71
78	433	7200	0.0697	0.015099	-21.29
79	443	7200	0.1068	0.015366	-20.84
80	453	7200	0.1589	0.015762	-20.43
81	463	7200	0.2312	0.016339	-20.02
82	473	10800	0.4853	0.017549	-19.63
83	483	7200	0.4399	0.018647	-19.26
84	493	9000	0.7322	0.020473	-18.89
85	500	7200	0.6851	0.022181	-18.65
86	496	7200	0.5364	0.023519	-18.83
87	486	7200	0.3489	0.024389	-19.21
88	476	7200	0.2248	0.024950	-19.62
89	466	7200	0.1486	0.025320	-20.01
90	456	7200	0.0980	0.025565	-20.42
91	464	7200	0.1319	0.025894	-20.11
92	474	7200	0.1955	0.026381	-19.70
93	484	7200	0.2814	0.027083	-19.31
94	494	7200	0.3972	0.028074	-18.94
95	500	7200	0.4744	0.029257	-18.72
Final			389.2381	1	
Total			400.9691		
			BR231 Orthogonal		
1	150	7200	0.1279	0.000503	-24.31
2	160	7200	0.0344	0.000638	-24.81
3	170	7200	0.0157	0.000700	-25.44
4	180	7200	0.0109	0.000742	-25.73
5	190	7200	0.0105	0.000784	-25.71
6	200	7200	0.0113	0.000828	-25.57
7	210	7200	0.0118	0.000874	-25.48
8	220	7200	0.0134	0.000927	-25.29
9	230	7200	0.0158	0.000989	-25.07
10	240	7200	0.0178	0.001059	-24.88
11	250	7200	0.0200	0.001138	-24.70
12	260	7200	0.0233	0.001229	-24.47
13	270	7200	0.0274	0.001337	-24.23
14	280	7200	0.0328	0.001466	-23.96
15	290	7200	0.0409	0.001627	-23.64
16	300	7200	0.0525	0.001833	-23.28
17	310	5400	0.0491	0.002026	-22.95

TABLE 3
(continued)

Step	T °C	seconds	^{4}He (pmol)	$f_{cumulative}$	$\ln(D/a^2)^1$
		BR231 Orthogonal			
19	330	5400	0.0777	0.002559	-22.27
20	340	3600	0.0709	0.002838	-21.84
21	350	3600	0.0970	0.003219	-21.41
22	360	3600	0.1234	0.003704	-21.03
23	370	3600	0.1547	0.004312	-20.66
24	380	3600	0.1881	0.005052	-20.31
25	390	3600	0.2706	0.006116	-19.77
26	400	3600	0.3494	0.007490	-19.32
27	410	3600	0.3823	0.008993	-19.04
28	420	3600	0.5844	0.011290	-18.40
29	430	3600	0.5252	0.013355	-18.32
30	440	3600	0.7263	0.016210	-17.81
31	450	3600	0.7794	0.019274	-17.56
32	460	3600	0.9852	0.023147	-17.14
33	470	3600	1.1924	0.027835	-16.77
34	480	3600	1.3463	0.033128	-16.47
35	490	1800	0.8142	0.036328	-16.15
36	500	1800	1.0398	0.040416	-15.80
37	500	1800	0.8920	0.043923	-15.86
38	495	1800	0.7145	0.046732	-16.01
39	485	3600	0.9032	0.050283	-16.40
40	475	2760	0.4327	0.051984	-16.82
41	465	3600	0.3922	0.053526	-17.15
42	455	3600	0.2576	0.054539	-17.55
43	445	3600	0.1638	0.055183	-17.99
44	435	3600	0.0986	0.055570	-18.49
45	425	3600	0.0624	0.055816	-18.94
46	415	3600	0.0424	0.055983	-19.32
47	405	3600	0.0260	0.056085	-19.81
48	395	3600	0.0146	0.056142	-20.38
49	385	3600	0.0114	0.056187	-20.63
50	375	3600	0.0074	0.056216	-21.07
51	365	7200	0.0083	0.056249	-21.63
52	355	7200	0.0051	0.056269	-22.13
53	345	7200	0.0028	0.056280	-22.74
54	335	14400	0.0033	0.056293	-23.27
55	325	21600	0.0029	0.056304	-23.79
56	315	43200	0.0030	0.056316	-24.45
57	305	43200	0.0020	0.056324	-24.85
58	295	52200	0.0012	0.056328	-25.56
59	285	95400	0.0014	0.056334	-25.99
60	275	86400	0.0009	0.056337	-26.35
61	265	93600	0.0006	0.056340	-26.82
62	273	86400	0.0017	0.056346	-25.74
63	283	86400	0.0016	0.056352	-25.79
64	293	86400	0.0021	0.056360	-25.51
65	303	54000	0.0016	0.056367	-25.32
66	313	54000	0.0037	0.056381	-24.47
67	323	21600	0.0020	0.056389	-24.15
68	324	25200	0.0037	0.056403	-23.71
69	343	21600	0.0022	0.056412	-23.09
70	353	7200	0.0038	0.056427	-22.41
71	363	7200	0.0065	0.056453	-21.87
72	373	7200	0.0111	0.056496	-21.34
73	383	7200	0.0203	0.056576	-20.74
74	393	7200	0.0314	0.056700	-20.30
75	403	7200	0.0486	0.056891	-19.86
76	413	7200	0.2473	0.057863	-18.22
77	423	7200	0.1493	0.058450	-18.72
78	433	7200	0.1959	0.059220	-18.43
79	443	7200	0.2856	0.060343	-18.04
80	453	7200	0.4981	0.062301	-17.46
81	463	7200	0.6177	0.064730	-17.21

TABLE 3
(continued)

Step	T °C	seconds	^{4}He (pmol)	$f_{cumulative}$	$\ln(D/a^2)^1$
			BR231 Orthogonal		
83	483	7200	1.2533	0.074861	-16.37
84	493	9000	2.2015	0.083516	-15.94
85	500	7200	1.9821	0.091308	-15.72
86	496	7200	1.6291	0.097713	-15.84
87	486	7200	1.0223	0.101732	-16.25
88	476	7200	0.6770	0.104393	-16.63
89	466	7200	0.4594	0.106199	-17.00
90	456	7200	0.2950	0.107359	-17.43
91	464	7200	0.4177	0.109001	-17.07
92	474	7200	0.5898	0.111320	-16.70
93	484	7200	0.8262	0.114568	-16.34
94	494	7200	1.1494	0.119086	-15.98
95	500	7200	1.3934	0.124564	-15.74
Final			222.6819	1	
Total			254.3670		
			M127 Parallel		
1	150	3600	0.2379	0.000057	-27.99
2	160	7200	0.1026	0.000081	-28.63
3	170	7200	0.0691	0.000097	-28.77
4	180	7200	0.0638	0.000113	-28.69
5	190	7200	0.0658	0.000128	-28.52
6	200	7200	0.0721	0.000145	-28.30
7	210	7200	0.0787	0.000164	-28.09
8	220	7200	0.0883	0.000185	-27.85
9	230	7200	0.0992	0.000209	-27.62
10	240	7200	0.1105	0.000235	-27.39
11	250	7200	0.1250	0.000265	-27.15
12	260	7200	0.1444	0.000299	-26.88
13	270	7200	0.1673	0.000339	-26.61
14	280	7200	0.1986	0.000386	-26.31
15	290	7200	0.2557	0.000447	-25.92
16	300	7200	0.3126	0.000521	-25.57
17	310	5400	0.2890	0.000590	-25.22
18	320	5400	0.3859	0.000682	-24.80
19	330	5400	0.4842	0.000797	-24.42
20	340	3600	0.4325	0.000900	-23.99
21	350	3600	0.5442	0.001030	-23.63
22	360	3600	0.7023	0.001197	-23.23
23	370	3600	0.8021	0.001388	-22.95
24	380	3600	1.0578	0.001639	-22.52
25	390	3600	1.3080	0.001951	-22.13
26	400	3600	1.5239	0.002313	-21.81
27	410	3600	1.7690	0.002734	-21.49
28	420	1800	1.1152	0.002999	-21.13
29	430	1800	1.7229	0.003409	-20.59
30	440	1800	1.7772	0.003832	-20.43
31	450	1800	2.0742	0.004326	-20.16
32	460	1800	2.5888	0.004942	-19.81
33	470	1800	3.1134	0.005683	-19.49
34	480	1800	3.2833	0.006464	-19.30
35	490	1800	3.6730	0.007338	-19.06
36	500	1800	4.9432	0.008514	-18.63
37	500	1800	3.8673	0.009434	-18.75
38	490	1800	2.4987	0.010029	-19.10
39	485	1800	1.9250	0.010487	-19.31
40	475	1800	1.2676	0.010788	-19.69
41	465	1800	0.8148	0.010982	-20.11
42	455	1800	0.5378	0.011110	-20.51
43	445	1800	0.3505	0.011194	-20.93
44	435	1800	0.2320	0.011249	-21.34
45	425	1800	0.1410	0.011282	-21.83

TABLE 3
(continued)

Step	T °C	seconds	^{4}He (pmol)	$f_{cumulative}$	$\ln(D/a^2)^1$
		M127 Parallel			
46	415	1800	0.0935	0.011305	-22.24
47	405	1800	0.0592	0.011319	-22.70
48	395	3600	0.0672	0.011335	-23.26
49	385	3600	0.0472	0.011346	-23.61
50	375	5400	0.0427	0.011356	-24.12
51	365	5400	0.0271	0.011363	-24.57
52	355	5400	0.0333	0.011371	-24.36
53	345	5400	0.0106	0.011373	-25.51
54	335	7200	0.0093	0.011375	-25.93
55	325	21600	0.0137	0.011379	-26.64
56	315	54000	0.0186	0.011383	-27.25
57	305	61200	0.0121	0.011386	-27.81
58	295	65040	0.0122	0.011389	-27.85
59	285	64800	0.0045	0.011390	-28.86
60	275	72180	0.0033	0.011391	-29.27
61	265	137400	0.0040	0.011392	-29.73
62	273	86400	0.0034	0.011392	-29.43
63	283	73800	0.0048	0.011393	-28.92
64	293	88200	0.0085	0.011395	-28.53
65	303	88200	0.0145	0.011399	-27.99
66	313	77400	0.0217	0.011404	-27.45
67	323	43200	0.0210	0.011409	-26.90
68	333	36060	0.0311	0.011416	-26.33
69	343	7200	0.0108	0.011419	-25.78
70	353	7200	0.0182	0.011423	-25.25
71	363	7200	0.0281	0.011430	-24.82
72	373	7200	0.0478	0.011441	-24.29
73	383	7200	0.0811	0.011461	-23.76
74	393	7200	0.1278	0.011491	-23.30
75	403	7200	0.2098	0.011541	-22.80
76	413	7200	0.3249	0.011618	-22.36
77	423	7200	0.5139	0.011741	-21.89
78	433	7200	0.7594	0.011921	-21.49
79	443	3600	0.5520	0.012053	-21.10
80	453	10800	2.4045	0.012625	-20.70
81	463	3600	1.1003	0.012887	-20.35
82	473	3600	1.5677	0.013260	-19.97
83	483	3600	2.0406	0.013745	-19.67
84	493	3600	2.8538	0.014424	-19.29
85	500	3660	3.4657	0.015249	-19.06
86	500	17400	13.6878	0.018506	-19.12
87	491	10800	5.6438	0.019849	-19.40
88	481	11400	3.5447	0.020692	-19.87
89	471	10800	2.1586	0.021206	-20.28
90	461	10800	1.5258	0.021569	-20.60
91	451	14400	1.2817	0.021874	-21.05
92	441	14400	0.8642	0.022079	-21.43
93	431	14400	0.5545	0.022211	-21.87
94	421	14400	0.3480	0.022294	-22.33
95	411	14400	0.2149	0.022345	-22.81
96	401	14400	0.1340	0.022377	-23.28
97	412	14400	0.2299	0.022432	-22.74
98	422	14400	0.3530	0.022516	-22.30
99	432	14400	0.5193	0.022639	-21.91
100	442	14400	0.7913	0.022828	-21.48
101	452	14400	1.2062	0.023115	-21.05
102	462	10800	1.2847	0.023420	-20.69
103	472	10800	1.8524	0.023861	-20.31
104	482	10800	2.6793	0.024499	-19.92
105	492	10800	4.7614	0.025632	-19.30
106	500	10800	4.4928	0.026701	-19.32
107	500	10800	8.0044	0.028605	-18.69
108	494	10800	4.2192	0.029609	-19.28

TABLE 3
(continued)

Step	T °C	seconds	^{4}He (pmol)	$f_{cumulative}$	$\ln(D/a^2)^1$
			M127 Parallel		
109	484	10800	2.9059	0.030301	-19.62
110	474	10800	1.8160	0.030733	-20.07
111	464	10800	1.1450	0.031005	-20.52
112	454	10800	0.7717	0.031189	-20.91
113	444	10800	0.5258	0.031314	-21.29
114	434	10800	0.3329	0.031393	-21.74
115	424	10800	0.2021	0.031441	-22.24
116	414	10800	0.1247	0.031471	-22.72
117	404	10800	0.0899	0.031492	-23.05
118	416	10800	0.1600	0.031530	-22.47
Remaining			4070.1621	1	
Total			4202.6738		
			M127 Orthogonal		
1	150	7200	0.4160	0.000213	-26.03
2	160	7200	0.1351	0.000282	-26.32
3	170	7200	0.1194	0.000343	-26.20
4	180	7200	0.1402	0.000415	-25.85
5	190	7200	0.1175	0.000475	-25.87
6	200	7200	0.1184	0.000535	-25.73
7	210	7200	0.1271	0.000600	-25.55
8	220	7200	0.1532	0.000679	-25.24
9	230	7200	0.1527	0.000757	-25.13
10	240	7200	0.1716	0.000844	-24.90
11	250	7200	0.1999	0.000947	-24.64
12	260	7200	0.1965	0.001047	-24.55
13	270	7200	0.2475	0.001174	-24.21
14	280	7200	0.2669	0.001310	-24.02
15	290	7200	0.3669	0.001498	-23.58
16	300	7200	0.3787	0.001692	-23.42
17	310	7200	0.4387	0.001916	-23.15
18	320	7200	0.5181	0.002181	-22.86
19	330	7200	0.6108	0.002493	-22.56
20	340	7200	0.7037	0.002853	-22.28
21	350	7200	0.8234	0.003274	-21.99
22	360	7200	1.1639	0.003869	-21.49
23	370	7200	1.2523	0.004510	-21.26
24	380	7200	1.4350	0.005244	-20.97
25	390	7200	1.7364	0.006132	-20.63
26	400	7200	1.9666	0.007137	-20.35
27	410	3600	1.1416	0.007721	-20.09
28	420	3600	1.4408	0.008458	-19.77
29	430	3600	1.7659	0.009361	-19.47
30	440	3600	2.1070	0.010438	-19.19
31	450	3600	2.4938	0.011714	-18.90
32	460	3600	2.8906	0.013192	-18.64
33	470	3600	3.2765	0.014867	-18.40
34	480	3600	3.7039	0.016762	-18.15
35	490	3600	4.1231	0.018870	-17.93
36	500	3600	4.5985	0.021222	-17.70
37	500	3600	4.2774	0.023409	-17.66
38	495	3600	3.0881	0.024988	-17.91
39	485	3600	1.9691	0.025995	-18.31
40	475	3600	1.2504	0.026635	-18.73
41	465	3600	0.8194	0.027054	-19.13
42	455	3600	0.5460	0.027333	-19.53
43	445	3600	0.3778	0.027526	-19.89
44	435	3600	0.2417	0.027650	-20.33
45	425	3600	0.1627	0.027733	-20.72
46	415	3600	0.1050	0.027787	-21.15
47	405	3600	0.1337	0.027855	-20.91
48	395	7200	0.0923	0.027902	-21.97

TABLE 3
(continued)

Step	T °C	seconds	^{4}He (pmol)	$f_{cumulative}$	$\ln(D/a^2)^1$
			M127 Orthogonal		
49	385	7200	0.0554	0.027931	-22.48
50	375	7200	0.0335	0.027948	-22.98
51	365	7200	0.0204	0.027958	-23.48
52	355	14400	0.0268	0.027972	-23.90
53	345	14400	0.0153	0.027980	-24.46
54	335	22020	0.0143	0.027987	-24.95
55	325	51000	0.0188	0.027997	-25.52
56	315	43200	0.0097	0.028002	-26.01
57	305	43200	0.0071	0.028005	-26.33
58	295	90000	0.0077	0.028009	-26.98
59	285	90000	0.0047	0.028012	-27.48
60	275	90900	0.0040	0.028014	-27.64
61	265	86400	0.0029	0.028015	-27.90
62	273	86400	0.0026	0.028017	-28.03
63	283	86700	0.0039	0.028019	-27.63
64	293	91800	0.0057	0.028021	-27.30
65	303	43200	0.0043	0.028024	-26.82
66	313	43200	0.0076	0.028028	-26.26
67	323	43200	0.0120	0.028034	-25.80
68	324	43200	0.0104	0.028039	-25.94
69	343	21600	0.0177	0.028048	-24.25
70	353	14400	0.0204	0.028059	-24.17
71	363	14400	0.0340	0.028076	-23.66
72	373	7200	0.0305	0.028091	-23.07
73	383	7200	0.0461	0.028115	-22.66
74	393	14340	0.1552	0.028194	-22.13
75	403	7200	0.1140	0.028253	-21.75
76	413	7200	0.1782	0.028344	-21.30
77	423	7200	0.2695	0.028482	-20.88
78	433	7200	0.4023	0.028687	-20.47
79	443	7200	0.6040	0.028996	-20.06
80	453	7200	0.8788	0.029446	-19.67
81	463	7200	1.5433	0.030235	-19.09
82	473	7200	2.1286	0.031323	-18.73
83	483	7200	2.7566	0.032733	-18.44
84	493	7200	3.4700	0.034508	-18.16
85	500	7200	4.1040	0.036606	-17.93
86	492	7200	2.7744	0.038025	-18.28
87	482	7380	1.8395	0.038966	-18.68
88	472	7200	1.2113	0.039585	-19.05
89	462	7200	0.8091	0.039999	-19.44
90	452	7200	0.8431	0.040430	-19.39
91	442	7200	0.5338	0.040703	-19.84
92	456	7200	0.9186	0.041173	-19.29
93	466	7200	1.3045	0.041840	-18.92
94	476	7500	1.9499	0.042837	-18.54
95	486	7200	2.4924	0.044112	-18.23
96	496	7200	3.2941	0.045796	-17.92
97	500	7200	3.4120	0.047541	-17.85
Final			1862.4845	1	
Total			1955.4491		
			G3 Orthogonal		
1	150	7200	1.0804	0.000373	-24.91
2	160	7200	0.5269	0.000555	-24.72
3	170	7200	0.5089	0.000730	-24.43
4	180	7200	0.5485	0.000920	-24.10
5	190	7200	0.6479	0.001143	-23.71
6	200	7200	0.8986	0.001453	-23.16
7	210	7200	1.3448	0.001917	-22.49
8	220	7200	2.0963	0.002641	-21.75
9	230	7200	3.1663	0.003733	-21.00

TABLE 3
(continued)

Step	T °C	seconds	^{4}He (pmol)	$f_{cumulative}$	$\ln(D/a^2)^1$
			G3 Orthogonal		
10	240	7200	4.7786	0.005382	-20.23
11	250	3600	3.5311	0.006601	-19.56
12	260	3600	5.1900	0.008392	-18.96
13	270	3600	7.4090	0.010949	-18.34
14	280	3600	10.1456	0.014450	-17.76
15	290	3600	12.9674	0.018925	-17.24
16	300	3600	16.6412	0.024667	-16.72
17	310	1800	10.7667	0.028383	-16.27
18	320	1800	14.1582	0.033268	-15.84
19	330	1800	17.6617	0.039363	-15.46
20	340	1800	21.9211	0.046928	-15.07
21	350	1800	27.1528	0.056298	-14.68
22	345	1800	21.1101	0.063583	-14.78
23	335	1800	13.7175	0.068316	-15.12
24	325	1800	9.5874	0.071625	-15.41
25	315	1800	6.4708	0.073858	-15.77
26	305	1800	8.4136	0.076761	-15.47
27	295	3600	5.6929	0.078726	-16.52
28	285	3600	4.0126	0.080110	-16.85
29	275	3600	2.4432	0.080953	-17.33
30	265	3600	1.5538	0.081490	-17.78
31	255	3600	0.9890	0.081831	-18.23
32	245	3600	0.6107	0.082042	-18.70
33	235	3600	0.3819	0.082173	-19.17
34	225	7200	0.4727	0.082337	-19.65
35	215	7200	0.2788	0.082433	-20.18
36	205	7200	0.1583	0.082487	-20.74
37	195	7200	0.0902	0.082518	-21.30
38	185	8100	0.0555	0.082538	-21.91
39	175	14700	0.0410	0.082552	-22.80
40	165	10800	0.0204	0.082559	-23.19
41	155	12600	0.0123	0.082563	-23.85
42	163	10800	0.0174	0.082569	-23.35
43	173	7200	0.0230	0.082577	-22.67
44	183	7200	0.0424	0.082592	-22.06
45	193	7200	0.0901	0.082623	-21.30
46	203	7200	0.1790	0.082685	-20.62
47	213	7200	0.2518	0.082771	-20.27
48	223	7200	0.4249	0.082918	-19.75
49	233	7200	0.6855	0.083155	-19.27
50	243	7200	1.1241	0.083543	-18.77
51	253	7200	1.7801	0.084157	-18.30
52	263	7200	3.0731	0.085217	-17.75
53	273	7200	4.2407	0.086681	-17.41
54	283	7200	6.4103	0.088893	-16.98
55	293	7200	9.0718	0.092023	-16.60
56	303	7200	12.8863	0.096470	-16.21
57	313	7200	17.5423	0.102524	-15.84
58	323	3600	12.1823	0.106728	-15.47
59	333	3600	16.0941	0.112281	-15.14
60	343	3600	21.2508	0.119615	-14.81
61	353	3600	27.6175	0.129145	-14.47
62	363	1800	18.5970	0.135563	-14.11
63	373	1800	24.1683	0.143903	-13.80
64	383	1800	30.7314	0.154508	-13.49
65	380	1800	27.2635	0.163916	-13.55
66	370	3600	38.0687	0.177053	-13.84
67	360	3600	26.7475	0.186283	-14.13
68	350	3600	19.4454	0.192993	-14.40
Final			2338.5778	1	
Total			2897.8419		

TABLE 3
(continued)

Step	T °C	seconds	^{4}He (pmol)	$f_{cumulative}$	$\ln(D/a^2)^1$
		N 17			
1	150	3600	35.2523	0.014650	-16.88
2	160	1200	9.4435	0.018575	-16.28
3	170	1200	11.8759	0.023510	-15.81
4	180	900	11.7131	0.028378	-15.33
5	190	900	14.4134	0.034368	-14.93
6	200	900	17.8751	0.041797	-14.52
7	210	900	22.5784	0.051180	-14.09
8	220	900	27.5532	0.062631	-13.69
9	230	600	25.6529	0.073292	-13.18
10	240	600	32.0131	0.086596	-12.79
11	250	600	40.3468	0.103363	-12.39
12	260	600	55.1423	0.126280	-11.89
13	270	600	71.0224	0.155796	-11.43
14	270	600	66.9108	0.183603	-11.30
15	265	600	56.9539	0.207272	-11.32
16	255	600	44.8586	0.225915	-11.46
17	245	600	33.5697	0.239866	-11.67
18	235	600	22.7868	0.249336	-12.01
19	225	600	16.1135	0.256032	-12.33
20	215	900	16.2080	0.262768	-12.70
21	205	900	11.2881	0.267459	-13.04
22	195	900	7.7815	0.270693	-13.40
23	185	900	4.8317	0.272701	-13.86
24	193	900	6.3944	0.275358	-13.58
25	203	900	9.6056	0.279350	-13.16
26	213	900	13.4569	0.284943	-12.80
27	223	600	13.3297	0.290482	-12.39
28	233	600	18.3729	0.298118	-12.04
29	243	600	24.6526	0.308363	-11.72
30	253	600	31.4894	0.321450	-11.44
31	263	600	39.7182	0.337956	-11.16
Final			1594.0053	1	
Total			2407.7036		
		TH 62Z^2			
1	310	5400	0.0079	0.003507	-22.34
2	350	5580	0.0112	0.008507	-20.79
3	375	4560	0.0116	0.013676	-19.94
4	400	5040	0.0182	0.021799	-19.12
5	425	3420	0.0163	0.029073	-18.48
6	450	4080	0.0372	0.045666	-17.45
7	475	3780	0.0363	0.061831	-16.99
8	500	5640	0.0686	0.092412	-16.37
9	480	9480	0.0357	0.108338	-17.26
10	460	18600	0.0376	0.125094	-17.72
11	440	17880	0.0132	0.130980	-18.62
12	420	45120	0.0168	0.138467	-19.25
13	395	86340	0.0138	0.144602	-20.04
14	495	4080	0.0139	0.150809	-16.93
15	510	4080	0.0238	0.161405	-16.33
16	520	3780	0.0273	0.173579	-16.03
17	530	3720	0.0383	0.190650	-15.58
18	540	3840	0.0441	0.210311	-15.36
19	410	228120	0.0395	0.227930	-19.45
Final			1.7316	1	
Total			2.2428		

[1] Values calculated from equations described in Fechtig and Kalbitzer (1966) assuming a plane sheet geometry.

[2] Values for $\ln(D/a^2)$ calculated from equations described in Fechtig and Kalbitzer (1966) assuming a spherical geometry.

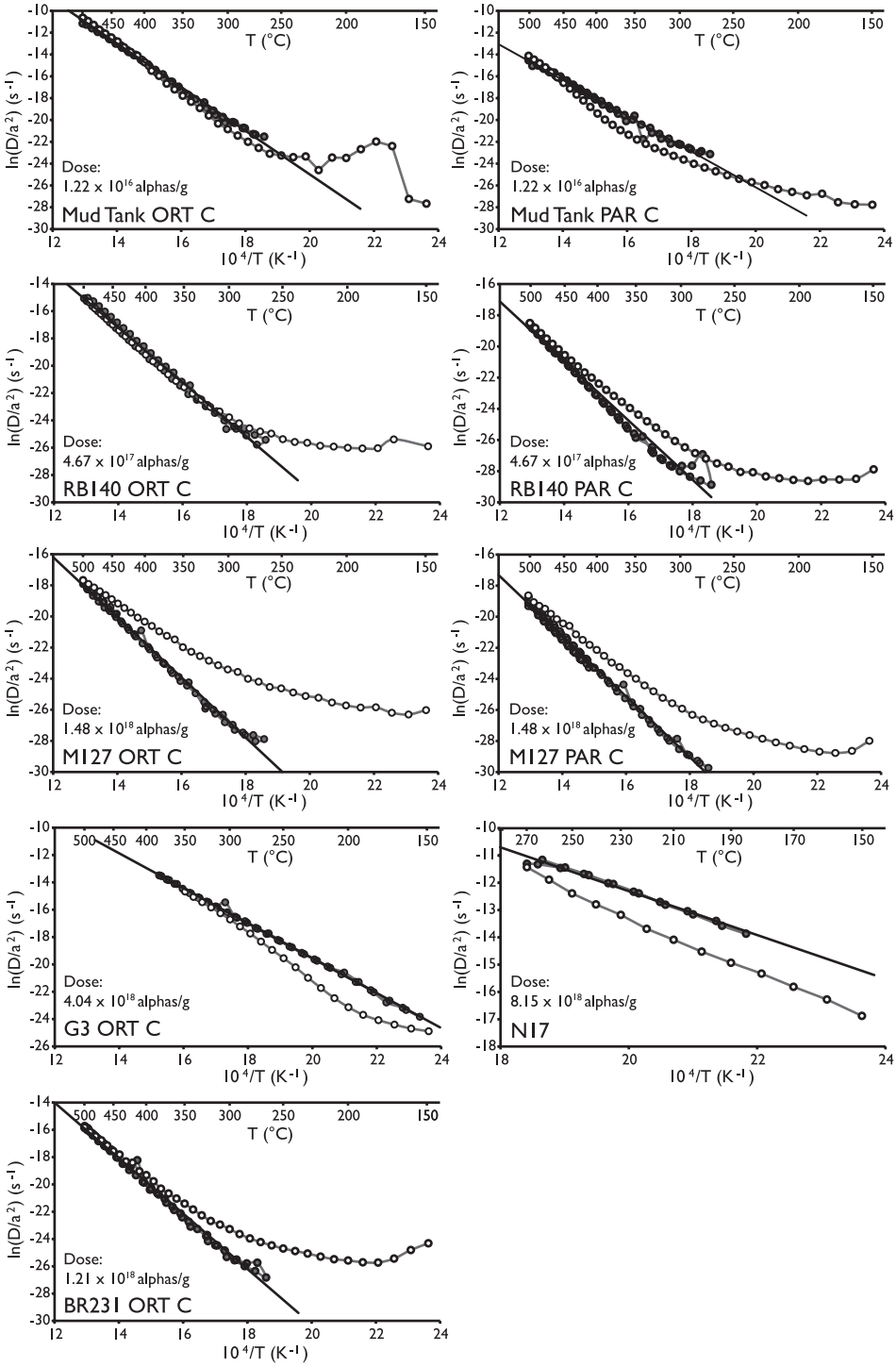

Fig. 3. Arrhenius plots for various zircon slabs. In both plots, non-linear trends are observed in the initial temperature steps (white markers). Linear regression for obtaining kinetic parameters performed on steps following the high-temperature reached in the initial prograde path (gray markers).

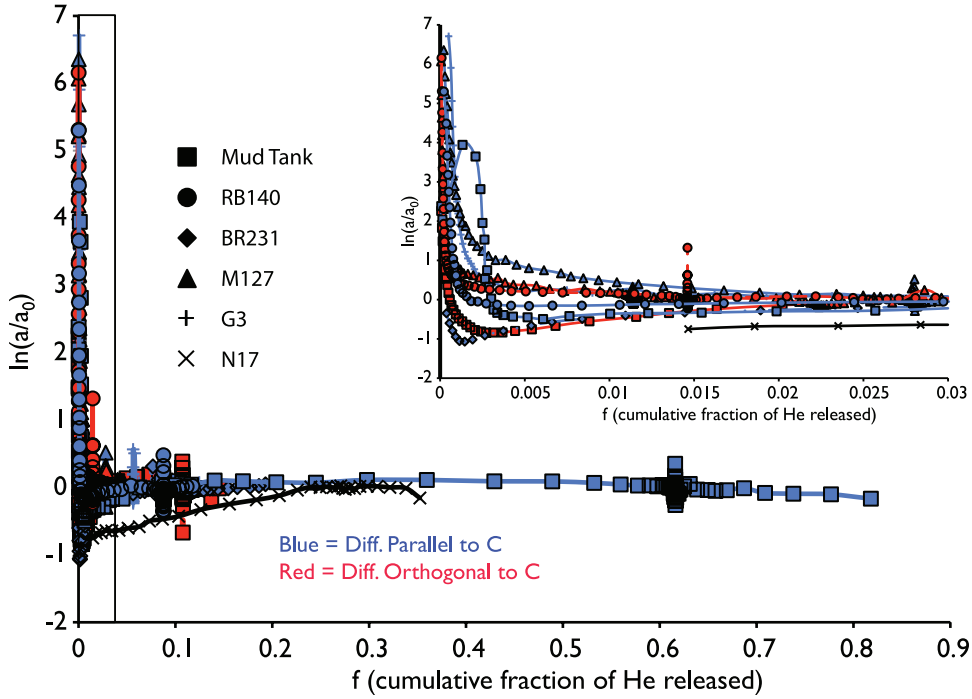

Fig. 4. Ln(a/a_0) plotted as a function of cumulative fraction of He released in step-heating experiments. This term describes the deviation of D/a^2 at any given time step from the D/a^2 determined from linear regression. See Reiners and others (2004) for the derivation. The inset is a magnified version of the main plot. The rectangular box in the main plot indicates the span of this inset. Despite the initial high deviation in ln(a/a_0) at low cumulative fraction released, almost all samples approach a value of 0 (no deviation) after roughly the first percent of gas is released.

this type of non-linear behavior was apparent in the lowest retrograde temperature steps of some slabs.

To derive kinetic parameters for each slab we linearly regress all steps following our initial highest temperature step. Table 4 shows the activation energy (E_a) and frequency factor/diffusion dimension (D_0/a^2) parameters we obtain from these post-high temperature steps assuming a plane sheet geometry. We also calculate frequency factors (D_0) using the half-width measurement for each slab and these are listed in table 4 as well. With the exception of one slab (Mud Tank PAR_C), values of E_a for all crystalline slabs show a relatively restricted range (155 to 172 kJ/mol), compared with the six order of magnitude range in frequency factors (5.03×10^{-3} to 146 cm^2/s). This large span in D_0 values is shown in figure 5. The ORT_C samples (oriented orthogonal to c-axis and dominated by c-axis parallel diffusion) in this study approximate a (log-log) linear relationship between D_0 and alpha dose. Most previously published D_0 values are also reasonably consistent with this trend except for one sample from Reiners and others (2002) (98PRGB4) and the two samples analyzed in Wolfe and Stockli (2010) (ZKTB4050 and ZKTB1516). Interestingly, D_0 values for the PAR_C samples in this study remain constant over much of the same range in alpha dose, as figure 5 highlights.

Figure 6 shows Arrhenius trends for each sample using the kinetics derived above. The difference in diffusivity between the oriented Mud Tank slabs is ~1 order of magnitude at the same temperature, but this pair has diffusivities that are roughly 3

TABLE 4

Kinetic parameters from step-heating experiments

Sample Name	Slab Orientation (relative to c)	log (D_0/a^2)	1σ	D_0 (cm^2/s)	1σ	E_a (kJ/mol)	1σ	T_c $a = 60$ μm (°C)[1]
Mud Tank	Orthogonal	6.6455	± 0.1071	110.5	+30.9 −24.2	167.93	± 0.68	132
Mud Tank	Parallel	3.0385	± 0.1568	0.0273	+0.0119 −.0083	138.22	± 0.99	126
RB140	Orthogonal	4.7014	± 0.1853	0.2011	+0.1070 −.0699	166.49	± 1.15	185
RB140	Parallel	3.0552	± 0.1504	0.0230	+0.0095 −.0067	166.19	± 0.97	207
BR231	Orthogonal	4.5667	± 0.1438	0.2304	+0.0905 −.0650	169.75	± 0.92	193
M127	Orthogonal	3.1172	± 0.1266	0.0265	+0.0090 −.0067	161.58	± 0.81	192
M127	Parallel	2.6729	± 0.1045	0.0265	+0.0072 −.0057	162.83	± 0.68	195
G3	Orthogonal	2.6320	± 0.0596	4.193×10^{-3}	+0.0007 −.0006	106.53	± 0.31	49
N17	n.a.	2.0538	± 0.0835	6.367×10^{-3}	+0.0013 −.0011	70.74	± 0.40	-59
TH62Z	n.a.	2.6738	± 0.2583	0.0170	+0.0138 −.0076	145.96	± 0.44	152

Note: 1σ uncertainties are calculated only from linear regression data after the end of the first prograde series of steps.
[1] Closure temperatures calculated with a spherical geometry for comparison to published results.

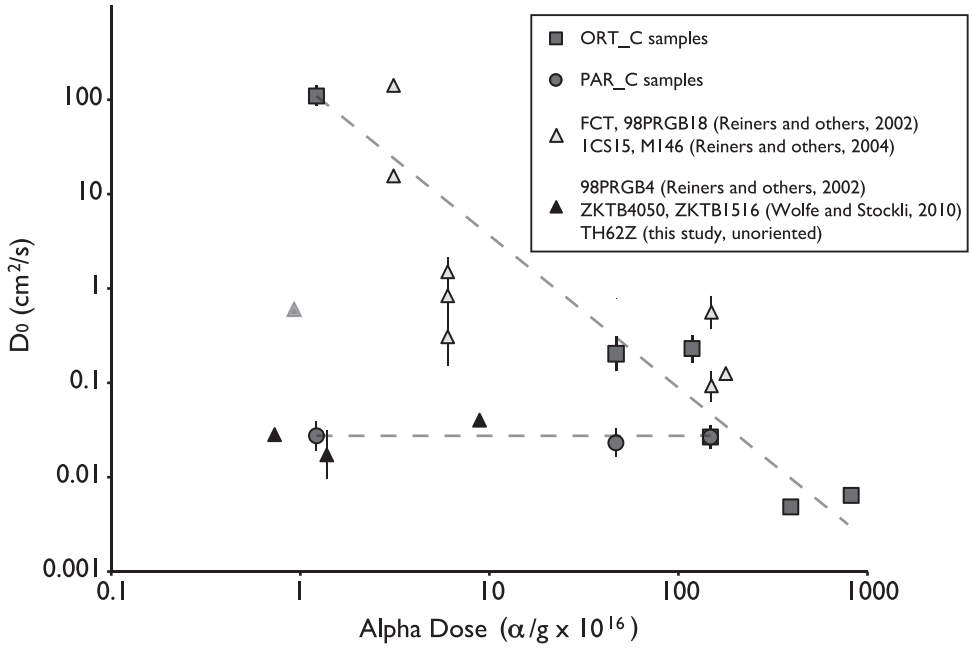

Fig. 5. Pre-exponential factor (D_0) versus radiation damage for samples analyzed in this study, and those previously published. Dashed lines have been added to highlight trends. Our ORT_C samples (all samples from this study with diffusion parallel to c-axis), as well as most of the published results, fall along a trend of decreasing D_0 with increasing radiation damage. The PAR_C samples (all samples from this study with diffusion orthogonal to c-axis), however, are constant with increasing damage. Also note that these two sets of values become similar at damage levels equivalent to those of M127. The previously published data mostly falls along one of these trends. We represent the data that agrees with our ORT_C samples in light gray triangles (FCT and 98PRGB18 from Reiners and others, 2002; and 1CS15 and M146 from Reiners and others, 2004), and the data that agrees with our PAR_C samples in black triangles (98PRGB4 from Reiners and others, 2002; and ZKTB4050 from Wolfe and Stockli, 2010). The gray triangle without a black border represents a single point that does not fall along either trendline (ZKTB1516 from Wolfe and Stockli, 2010). Error bars are for 1 sigma error, if reported (errors for some samples are not available).

orders of magnitude greater than the BR231, RB140, and M127 slabs. The RB140 pair of slabs also has only ~1 order of magnitude difference in diffusivities at the same temperature. Another pair of slabs, M127, shows almost no difference between the two directions (~0.1 log units). The parallel oriented RB140 slab and the orthogonally oriented RB140 slab have a difference in their diffusivities that is ~1 order of magnitude at the same temperature. In contrast, at higher alpha doses, the diffusivity of G3 (also orthogonally oriented) is roughly 6 orders of magnitude greater than that of BR231, and N17's diffusivity is approximately 10 orders of magnitude greater.

The relationship between alpha dose and diffusivity is more clearly demonstrated in figure 7, which shows diffusivity at a constant temperature (180 °C) as a function of alpha dose. In figure 8, we plot T_c as a function of alpha dose, an alternative, but equally effective visualization of the damage-diffusivity relationship as T_c combines both kinetic parameters into a single value that is more intuitive to practitioners of thermochronology. For completeness and comparison, we also include previously published results from unoriented zircons in figures 7 and 8 and calculate alpha doses from each sample's zircon He date (FCT, 98PRGB18, and 98PRGB4 from Reiners and others, 2002; 1CS15 and M146 from Reiners and others, 2004; and ZKTB4050 and ZKTB1516 from Wolfe and Stockli, 2010). Unfortunately, these previous studies did not control for the degree of radiation damage in each sample and we can only

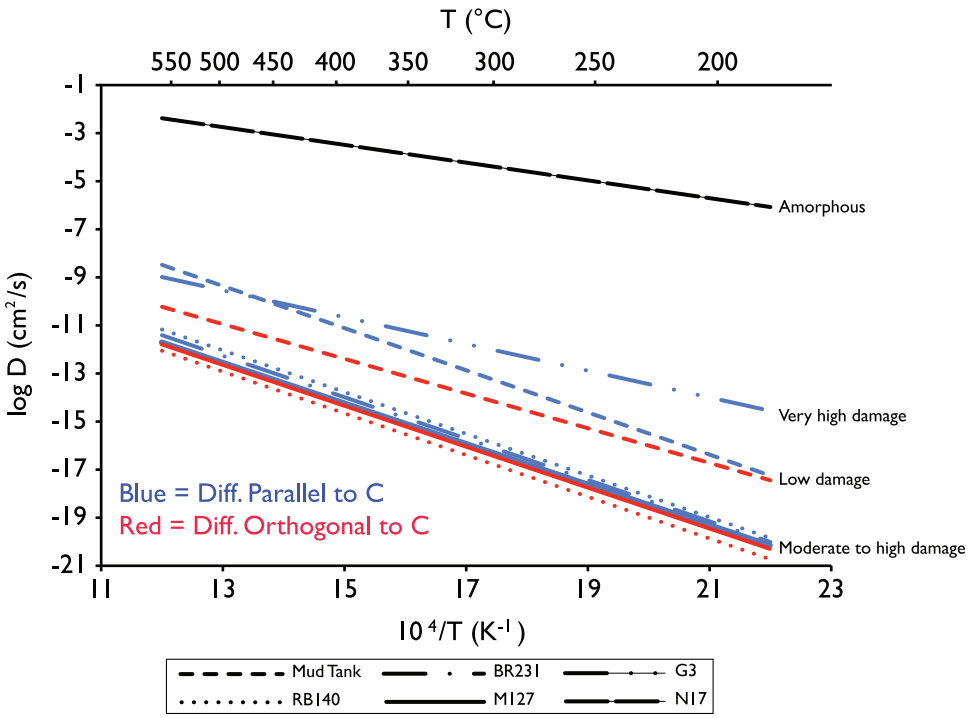

Fig. 6. Comparison of Arrhenius trends for samples shown in figure 4. Kinetic parameters used in this comparison are from post-high temperatures steps (blue markers in fig. 4). We have converted from values of D/a^2 to D using the half-width of each slab.

estimate damage when plotting these results. For samples with either simple thermal histories (FCT and 1CS15) or independent constraints on radiation damage (M146), alpha dose values derived from a zircon He date adequately describe the accumulated self-irradiation damage since damage was last annealed. However, for one sample, 98PRGB18, we used the U-Pb date to calculate alpha doses, which is appropriate given its thermal history.

Sample 98PRGB18 comes from a relatively shallow part of the Gold Butte block in Nevada, an ~15 km section of Mesoproterozoic crystalline rock that was rapidly exhumed by normal faulting at 15 to 16 Ma. This sample resided at only ~90 °C prior to Miocene exhumation (Reiners and others, 2000) and most likely never experienced temperatures high enough to fully anneal its radiation damage. Furthermore, the U-Pb derived alpha dose values for 98PRGB18 are generally consistent with some (but certainly not all) of the Raman spectra measured on different zircons from the same sample. Given internal zonation, radiation damage in this crystal is heterogeneous and we do not report a single value for FWHM. Instead, these values range from 3.6 to 16.5 cm^{-1} with a mean of 7.5 cm^{-1} (1001.5-1007.0 cm^{-1} shift). The higher values in this range are consistent with high amounts of radiation damage and it is possible that the diffusion data for 98PRGB18 comes from similar heavily damaged zircons.

Despite a less than ideal spread, these Raman data provide at least some estimate for damage in 98PRGB18, and can be compared to the Raman spectra from another sample from the same crustal block, 98PRGB4. This sample resided at much higher temperatures (likely >300 °C) prior to exhumation at 16 Ma (Reiners and others, 2000), and this date—coupled with U-Th concentrations in Reiners and others

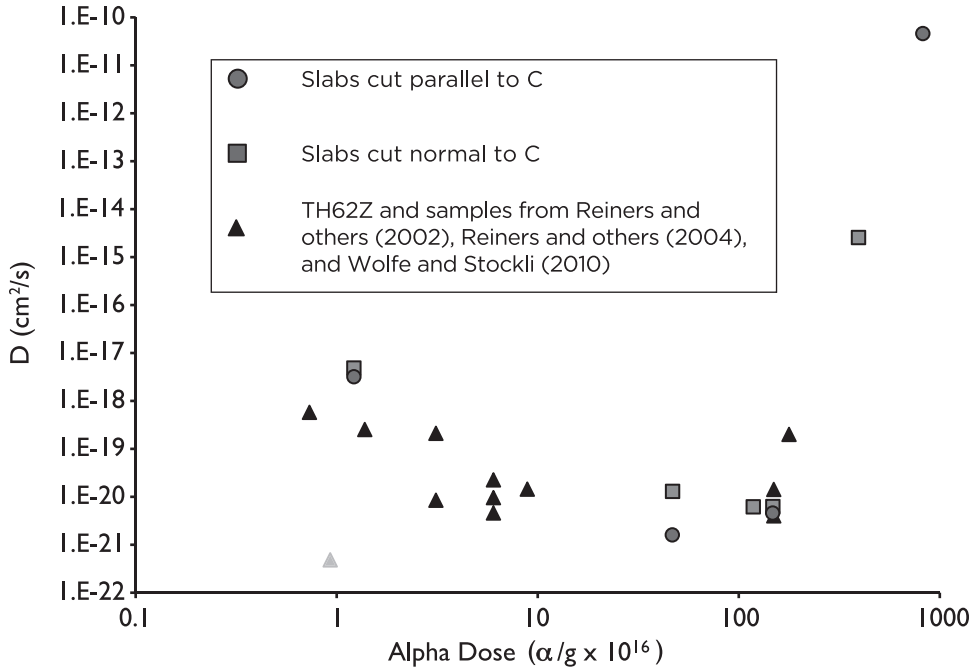

Fig. 7. Plot of He diffusivity versus alpha dose for samples described in figures 4 and 6, as well as samples whose kinetic parameters are already published. Temperature is held constant at 180 degrees Celsius. Gray triangle represent single sample from Wolfe and Stockli (2010) (ZKTB1516) that does not fall along our observed trend.

(2000)—yields an alpha dose similar to that of Mud Tank. Its FWHM values range from 2.8 to 10.9 cm^{-1} (1003.8-1007.5 cm^{-1} shift) with a mean of 5.7 cm^{-1} and are generally lower than 98PRGB18. Again, significant spread due to 98PRGB4's heterogeneous composition prevents us from assigning a single value for FWHM. Despite the complexity of these samples, Raman spectra give a best approximation of damage levels in 98PRGB18 and 98PRGB4 and some of these spectra are generally consistent with a zircon He date calculated alpha doses in 98PRGB4, and a zircon U-Pb date calculated alpha doses in 98PRGB18.

With these calculated alpha doses, our new diffusion data, as well as almost all previously published kinetics (with the exception of ZKTB1516), define the following relationship between He diffusion (at any T) and alpha dose: Between $\sim 1 \times 10^{16}$ to $\sim 5 \times 10^{17}$ α/g, diffusivity decreases by nearly three orders of magnitude. Diffusivity then increases again by as much as roughly 10 orders of magnitude at damage extents of N17 (fig. 7).

DISCUSSION

In the following sections, we develop a model for He diffusion in zircon that explains both our diffusion experiment results and the date-eU correlations in the context of the alpha dose-diffusivity relationship. We first describe an hypothesis that accounts for the physical significance of both types of date-eU correlations and provides the theoretical framework for our subsequent model derivation and parameterization. For this hypothesis we interpret positive correlations as a consequence of isolated radiation damage zones acting as impediments to He diffusion by increasing the tortuosity of diffusion pathways. In contrast, we interpret negative date-eU correla-

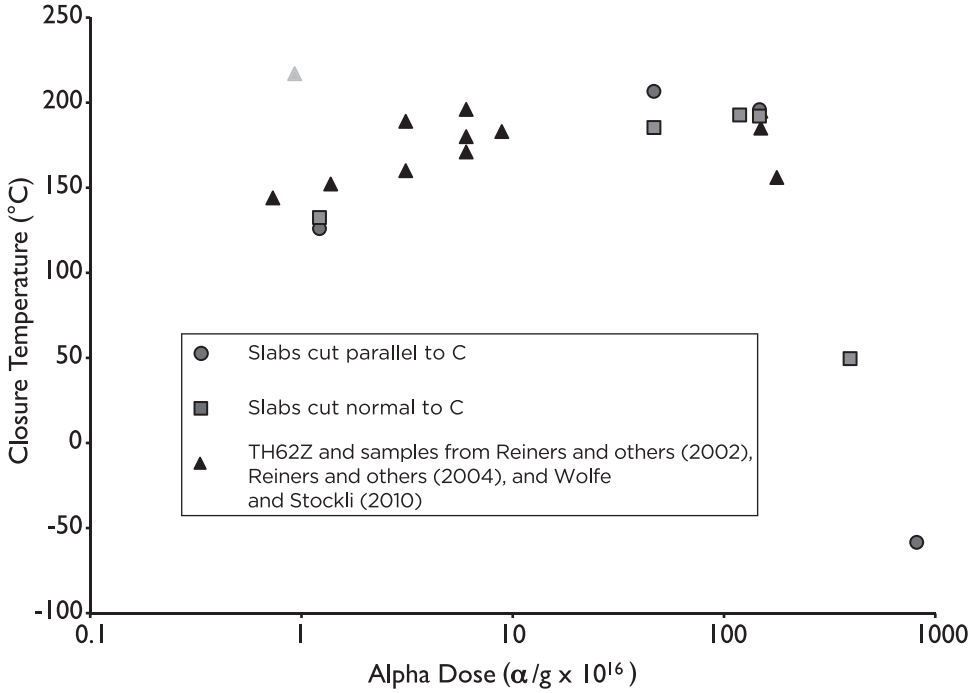

Fig. 8. Plot of closure temperature versus alpha dose for samples described in figures 4 and 6, as well as samples whose kinetic parameters are already published. Closure temperatures were calculated using a spherical geometry, diffusion domain size of 60 microns, and cooling rate of 10 °C/my. Gray triangle represents single sample from Wolfe and Stockli (2010) (ZKTB1516) that does not fall along our observed trend.

tions as a result of interconnection of damage zones at moderate to high alpha doses ($>2 \times 10^{18}$ α/g), as is qualitatively consistent with previous observations of increased He diffusion in highly damaged zircon (Holland, 1954; Hurley, 1954; Nasdala and others, 2004a).

Positive Date-eU Correlations

Due to similarities between our positive correlations and those observed with the apatite (U-Th)/He thermochronometer (for example, Flowers and others, 2007; Flowers and others, 2009; Flowers and Kelley, 2011), the effects of radiation damage on He diffusion in apatite provide context for interpreting zircon He positive correlations. Shuster and others (2006) showed that He diffusivity in apatite decreased with increasing damage and subsequent studies (for example, Flowers and others, 2007) supported this conclusion with observations of positive date-eU correlations. We suggest that similar behavior occurs in zircon and leads to positive date-eU correlations. For example, in the context of a thermal history like that depicted in figure 9, grains with different amounts of radiation damage, as well as an initial span of uniform dates, are reset to varying degrees during a reheating event (fig. 9A). If eU is a proxy for the total accumulated radiation damage (that is, all the zircons in a sample have experienced the same *t-T* history), then those grains with low eU lose a larger fraction of their He, resulting in a younger date, than grains with high eU, leading to a positive correlation. Samples that have undergone slow, monotonic cooling may also exhibit positive correlations. If a sample spends a significant amount of time at temperatures

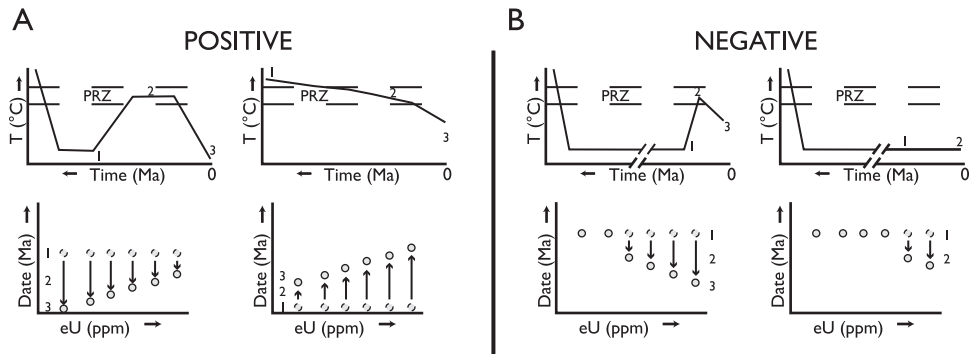

Fig. 9. Schematic of possible time-temperature paths that produce date-eU relationships. The arrows on each plot's axes indicate the direction in which the given value increases. Varying eU contents lead to differential accumulations of radiation damage, which in turn lead to differential He diffusivities. (A) If accumulation is relatively low, and a sample experiences a thermal pulse, or cools slowly through the PRZ so that damage in-growth and diffusion happen simultaneously, then a positive correlation results. (B) Conversely, if damage accumulation is relatively high (due to older zircons), then a thermal pulse results in a negative correlation, or significant He loss may occur at low temperatures.

low enough for damage accumulation without annealing, but high enough to be in the PRZ, then arrays of zircon He dates may form a positive correlation (fig. 9A). Both scenarios demonstrate that this correlation results from a sample with grains that span a range in eU, and have resided in the PRZ after disparate amounts of damage have accumulated in those grains.

A key difference between our interpretation of the damage-diffusivity relationship in zircon and the interpretation for the apatite system, though, is the mechanism that we suggest causes diffusivity to decrease with increasing damage. In the apatite He system, the decrease in He diffusivity is hypothesized to result from accumulation of crystal defects caused by alpha recoil damage that act as He traps. These traps sequester He (governed by an equilibrium partition coefficient) and prevent or slow its diffusive migration out of the crystal (Farley, 2000). In contrast to He diffusion in apatite, various authors (Farley, 2007; Reich and others, 2007; Saadoune and others, 2009) have demonstrated that He diffusion in an ideal or defect-free zircon should occur almost solely along c-axis parallel channels [0 0 1]. Any disruption of these pathways would force He through c-axis orthogonal openings ([1 0 0], [0 1 0], and [1 0 1]), which are much less energetically favorable (Reich and others, 2007). We argue that decreases in He diffusivity in zircon are largely due to the increasing disruption of diffusion fast-paths (c-axis parallel channels) by radiation damage, an effect similar to road blocks being placed on a major highway. As these barriers are erected inside the zircon, a He atom's path becomes more tortuous and the effective diffusivity of the grain decreases. Evidence for this increasing disruption of c-axis parallel channels comes from figure 5. The D_0 values for orthogonal oriented slabs (diffusion predominantly in the c-axis parallel direction) decrease across the damage spectrum whereas the D_0 values for the parallel oriented slabs (diffusion predominantly in the c-axis orthogonal direction) remain the same, with both sets of D_0 values becoming similar at high damage. In other words, diffusion kinetics in the orthogonal direction begin to more closely resemble diffusion kinetics in the parallel direction with increasing damage, and this increasing similarity can be explained by tortuosity. Tortuosity may also contribute to lowering He diffusivities in apatite, but we envision this phenomenon is more important for He diffusion in zircon due to its strongly anisotropic

behavior in specimens with little or no accumulated damage. We do not rule out that damage zones in zircon may also trap some amount of He, but we suggest that this effect is secondary compared to the closing of preferred diffusion directions, which are probably not present in apatite.

Negative Date-eU Correlations

Like the positive date-eU correlations, previous research provides some context for interpreting our negative date-eU correlations. Various authors (Holland, 1954; Hurley, 1954; and Nasdala and others, 2004a) have suggested that He diffusivities increase abruptly once zircon reaches a certain threshold of radiation damage. As damage increases, Reiners (2005) proposed that zircon He dates scale with the remaining crystalline fraction of the zircon as determined by the double-overlapping cascade model (Gibbons, 1972). This further suggests that above a threshold, interconnected damage zones form through-going channels in the zircon lattice and create fast diffusion pathways for He. In order to reach this interconnection or percolation threshold, zircons must sustain long-term damage accumulation at temperatures low enough to prevent annealing. Zircons may achieve a heavily damaged state in which either significant He loss and resetting occurs at surface temperatures, or some brief, low-temperature reheating event may cause resetting (fig. 9B). In detail, some amount of less diffusive material must remain in heavily damaged zircons as most negative correlations are gradual (that is Minnesota River Valley, Bighorn suite) and not so abrupt. However, in general, both scenarios could result in negative correlations and are plausible explanations for the datasets plotted in figure 2. Two of these samples, the Minnesota River Valley and Bighorn suites, come from Archean rocks that have likely been within a few kilometers of the surface for 10^8 to 10^9 years and have consequently accumulated large amounts of radiation damage. The Sri Lankan zircons are not as old but some do have high eU, which in some cases resulted in the complete breakdown of crystal structure (for example N17, Nasdala and others, 2004a).

The Sri Lankan dataset also shows a potential percolation threshold effect whereby dates are fairly reproducible up to a critical eU concentration, in this case about 2000 ppm eU, above which they decrease with increasing eU. The Cooma date-eU trend reinforces the notion of a transition in diffusion behavior as it displays both a positive and negative correlation with an abrupt transition between each. Damage in-growth since granulite facies metamorphism at ~433 Ma (Williams, 2001) and a large disparity in eU concentration (~100-1300 ppm) produced a suite of zircons in which two different processes affected He diffusion in different parts of the eU spectrum. In this particular dataset, the transition between the two types of He diffusion occurs at an eU of ~1000 ppm. Similarly, nearly all zircons in our positive correlations contain eU concentrations below 1000 ppm. The Cooma dataset serves as an important demonstration of how radiation damage may have contrasting effects on He diffusivity in a suite of grains from a single sample, and shows the approximate concentration of eU over which a transition from one process to the other may occur. Because both types of diffusion mechanism may operate on the same sample, these samples underscore the necessity for understanding the damage-diffusivity relationship across the entire damage spectrum.

Arrhenius Trends

There are a number of possible explanations for the non-linear portions of the Arrhenius plots in figure 4. Some of these plots show concave-up trends in the initial prograde steps, in which less than ~1 to 2 percent of the He is released. In contrast, subsequent temperature steps show much less variation and are more nearly linear. These concave-up trends can either plot above or below the linear Arrhenius trends. This feature, or ones similar to it, has been observed previously in zircon (Reiners and

others, 2002; Reiners and others, 2004) and several other minerals, including titanite (Reiners and Farley, 1999), goethite (Shuster and others, 2005), magnetite (Blackburn and others, 2007), and apatite (Farley, 2000). It has been attributed to inhomogeneous He distributions due to zonation, alpha ejection, or initial diffusion rounding; surface roughness; multiple diffusion domains; and radiation damage (for example, Reiners, 2005).

Despite the myriad possible causes, samples with concave-up curves that lie above the linear trends (RB140, BR231, and M127) are still difficult to explain. Anisotropy could produce non-Arrhenius behavior of this type in step-heating results if activation energies of the contrasting diffusion directions are different (Reich and others, 2007; Watson and others, 2010; Bengston and others, 2012). However, our data, as well as all other experimental He diffusion data on zircon or zircon-structure phases (Farley, 2007; Cherniak and others, 2009), indicate that anisotropy is manifest as differences in frequency factor, not activation energies, which would not lead to significant departure from linearity on an Arrhenius plot. Furthermore, if anisotropy in zircon was caused by differences in activation energy, then large changes in slope should always be evident at low temperatures regardless of how many prograde and retrograde cycles have been performed. For the most part, we do not observe this. We therefore rule out anisotropy as the source of non-Arrhenius behavior in our initial prograde temperature steps.

Reiners and others (2002) suggested that this type of non-Arrhenius behavior could be due to the interaction between radiation damage zones and the zircon surface, with the damage zones acting as grain boundaries or fast diffusion pathways. Recent evidence of two diffusion pathways for Ar in quartz (Clay and others, 2010), as well as investigations of fast path diffusion in other minerals (Yund and others, 1981; Yund and others, 1989; Yurimoto and others, 1989; Worden and others, 1990; Hacker and Christie, 1991) are consistent with this. For example, because lattice diffusion generally has a higher E_a than grain boundary diffusion (Chakraborty, 2008), lattice diffusion can be faster at high temperatures, so diffusion from grain-boundary-like domains could dominate gas release in early, prograde steps, yielding initially high diffusivities in Arrhenius plots. With higher temperature steps increasing fractions of gas would derive from lattice diffusion as a result of the difference in values of E_a, but also because surficial grain-boundary-like sites would be rapidly depleted in the initial few tenths to one percent of gas released (fig. 4). If grain-boundary-like sites were reoccupied with He during high temperature steps, this could also explain persistent release of gas via grain boundary diffusion in later steps. Arrhenius trends for M127, Mud Tank, RB140, and BR231 appear to exhibit slight curvature at the lowest temperatures of the post-high temperature heating steps (after initial 500 °C step), consistent with this explanation.

Concave-up curves that lie below the linear Arrhenius trends (Mud Tank, G3, and N17) probably result from a combination of the behavior described above and initially rounded He profiles. N17, with a closure temperature below 0 °C, likely possessed a rounded concentration profile prior to being step-heated, and, despite our selection of interior parts of the Mud Tank and G3 zircons, some portion from the rounded diffusion profile of these two samples was included as well. Although the initial He released from these zircons does not appear to conform to ideal expectations of simple Arrhenius behavior, its effect after the first few percent of gas release (except for N17) is negligible.

Functional Form for Damage-Diffusivity Relationship

For the remainder of our discussion, we directly relate alpha dose to structural damage, and derive a mathematical parameterization of the damage-diffusivity relationship that fits the data in figure 7. This requires a number of assumptions. As previously stated, we assume that alpha doses calculated from He ages sufficiently reflect the total

accumulation of alpha-decay events since structural damage was last annealed. Because most of our diffusion samples have thermal histories involving a phase of relatively rapid cooling, and because we have direct and independent measurements of a proxy for structural damage (FWHM) for a subset of them, this is a reasonable assumption.

We must also assume that He diffusion in zircon scales with both alpha dose and structural damage in the same way. This is an important consideration as alpha dose is a calculated damage proxy and not a direct measure of damage (we detail below the reasons for using alpha dose). We again rely on observations from the apatite He system to support this assumption. Shuster and Farley (2009) showed that the amount of ionizing kinetic energy released into a sample (kerma) and the fission-track density had similar effects on He diffusivity. They demonstrated that He diffusivity in apatite changes systematically with both increasing and decreasing kerma (through annealing) caused by either artificial irradiation or natural, self-irradiation as monitored by fission track density. Flowers and others (2009) expanded on this and derived a term, effective spontaneous fission track density, that directly related alpha dose, accumulation and annealing of fission tracks, and He diffusivity. Unfortunately, experimental observations analogous to those of Shuster and Farley (2009) are currently lacking for zircon. But both of these studies suggest that, at least to first order, fission track density (which is itself a measure of one type of structural radiation damage) scales with "effective alpha dose," and can therefore be related to bulk He diffusivity.

Finally, we are assuming that the negative correlation between alpha dose and diffusivity at low doses is not due to the effects of He (or Pb) concentration on He diffusivity. Shuster and Farley (2009) clearly showed that radiation damage, not He concentration, controls diffusivity in apatite. But as stated above, the types of experiments performed by Shuster and Farley (2009) do not yet exist for zircon, so we cannot completely rule out a concentration-dependency for He diffusion. However, the data of Shuster and Farley (2009) provide some confidence that similar processes are occurring in zircon, and this could be confirmed in the future by applying their methodology to zircon samples.

Although these assumptions are required, we suggest that linking alpha doses (preferentially those calculated using FT or He ages) to radiation damage is an appropriate choice for our purposes as these assumed "effective alpha doses" provide a straight-forward method for calculating damage accumulation through time. Furthermore, as we detail below, it provides a crucial link between equations describing He diffusivity and those describing damage annealing. The alpha dose is therefore the best measurement for integrating He diffusion, damage accumulation, and damage annealing over geologic timescales into an easily accessible thermochronometric modeling tool, which is our primary objective in this section. With this in mind, we first derive a parameterization for the damage-diffusivity relationship and then integrate this parameterization into a He diffusion and damage annealing numerical model.

A mathematical description of the damage-diffusivity relationship must account for both the initial decrease and ultimate increase in diffusivity across the spectrum of damage from at least Mud Tank to N17 ($\sim 10^{16}$-10^{19} α/g). These two samples represent the damage range encountered for the vast majority of zircon crystals sampled at or near the Earth's surface. We desire a functional form consistent with the hypothesis that decreasing diffusivity at low damage is caused by accumulation of isolated damage zones that block crystallographically preferred He transport pathways and increase the tortuosity of He migration. At high alpha doses, increasing diffusivity would be due to decreasing effective domain size of undamaged zircon volumes, which are increasingly separated by interconnected fast-diffusing damage zones.

In order to explain decreasing diffusivity at low damage, we introduce an effective diffusivity (D_e) that represents He diffusion in a damage-free lattice modified by

increasing tortuosity. Increasing radiation damage blocks or constricts easy He migration paths (for example, c-axis parallel channels) forcing He to take a more tortuous path out of the zircon. This is analogous to diffusion in a porous medium where effective diffusivity is expressed as (Cussler, 1984):

$$D_e = \frac{D_z}{\tau}. \tag{1}$$

D_z is the diffusion coefficient within the pores, or in our case, diffusion along c-axis pipes in a pristine zircon, and τ is the tortuosity. We represent D_z with the diffusion kinetics from a minimally damaged zircon. For this zircon's D_0, we fit the ORT_C slabs in figure 5 with a power-law relationship that yields an equation of $y = 134.89{*}x^{-1.578}$, where y is D_0 and x is dose. Projecting this relationship down to 1×10^{14} α/g gives a D_0 of 193188 cm^2/s (all constants and their values described in the remaining text are listed in table 5). For the E_a, we average the activation energies from the samples with minimal amorphous fractions (all samples excluding G3 and N17) and the previously published results. Although these parameters are both extrapolations, the following equations could be easily modified to account for future diffusion data from less damaged or more appropriate zircon specimens.

Tortuosity τ could be represented in a variety of ways, and the atomic-scale processes by which radiation damage may affect migration pathway dimensions and diffusivity are complex. Damage may displace atoms into open channels that, depending on which species is displaced, could cause variable decreases in porosity. C-axis channels of initially high ionic porosity could be completely blocked and a larger fraction of the He migration path would be forced to occur orthogonal to the c-axis. Although the exact geometry or porosity of damage zones is hard to constrain, we predict that most zones should act as He barriers and τ should increase as the chance increases for diffusing He atoms to encounter these barriers. To model this behavior, we use a metric introduced by Ketcham and others (2013) for characterizing the undamaged portion of the lattice, mean intercept length, l_{int}, which is the average distance a particle can travel in a single direction without encountering a damage zone. The expression for τ relates the calculated l_{int} in a given zircon to the mean intercept length in our extrapolated, minimally damaged zircon, which also displays high diffusivity ($l_{\mathrm{int}\,0}$):

$$\tau = \left(\frac{l_{\mathrm{int}\,0}}{l_{\mathrm{int}}}\right)^2. \tag{2}$$

The right-hand side of equation (2) is squared in part to improve the fit to our diffusion data (see below), but tortuousity is often mathematically expressed as the square of pore spacing or geometry (for example, Epstein, 1989). Ketcham and others (2013) have derived an empirical relation for l_{int} by modeling the accumulation and percolation of chains of connected, capsule-shaped alpha recoil tracks. They express l_{int} as a function of fraction amorphous (f_a):

$$l_{\mathrm{int}} = \frac{4.2}{f_a SV} - 2.5 \tag{3}$$

where SV corresponds to the surface to volume ratio of the capsules (1.669 nm^{-1}). In turn, f_a is described using the direct impact model (Gibbons, 1972):

$$f_a = 1 - \exp(-B_a \alpha) \tag{4}$$

TABLE 5

Constants and values used in parameterization

Symbol	Description	Value (Units)	Equation
D_z	Diffusivity of zircon with dose of 1 x 10^{14} α/g (see text for details)	E_a=165 (kJ/mol), D_0=193188 (cm^2/s)	1,5,7,8
l_{int0}	Mean intercept length of zircon with dose of 1 x 10^{14} α/g	45920 (nm)	2,8
SV	Surface area to volume ratio for damage capsules	1.669 (nm^{-1})	3
B_a	Mass of amorphous material produced per alpha decay event	5.48 x 10^{-19} (g/α-event)	4,6
D_{N17}	Diffusivity of amorphous material (N17 kinetics)	E_a=71 (kJ/mol), D_0=6.367 x 10^{-3} (cm^2/s)	5,7,8
Φ	Parameterization constant for amorphous fraction interconnectivity	3 (n.a.)	6
β	Damage annealing model parameter	-0.05721 (n.a.)	11
C_0	Damage annealing model parameter	6.24534 (n.a.)	11
C_1	Damage annealing model parameter	-0.11977 (n.a.)	11
C_2	Damage annealing model parameter	-314.937 (n.a.)	11
C_3	Damage annealing model parameter	-14.2868 (n.a.)	11

where B_a is the mass of amorphous material produced per alpha decay (5.48×10^{-19} g/α-event), and α is the alpha dose.

An explanation for the increase in diffusivity at high damage requires a derivation that accounts for interconnected amorphous zones. We hypothesize that at sufficiently high self-irradiation levels, amorphous zones caused by damage become interconnected and connected to the grain's surface. This represents an important shift from damage zones acting as barriers to damage zones acting as fast paths. The processes by which this might occur are not entirely apparent. Various macroscopic and long-range order properties change at high damage and track with amorphous fraction (for example, Ewing and others, 2003) and we expect that diffusivity should as well. However, several different atomistic processes may cause these changes. Devanathan and others (2006) showed that damage zones are characterized by an amorphous core surrounded by a high interstitial density rind. These amorphous cores could become connected at high damage and may form fast paths while the rinds cause increasing tortuosity at lower damage. Interconnected fission tracks, which only reach a percolation threshold at high damage (Ketcham and others, 2013) are another candidate for creating these fast paths (see below). Regardless of the exact mechanism, the net effect of this process is creation of an increasing number of progressively smaller, undamaged zones that are increasingly isolated from one another by increasingly interconnected and progressively larger damage zones with much higher diffusivity. These two effects can be accounted for by 1) modeling a decrease in the size of the diffusion domain of the undamaged portion of the grain, and 2) describing the bulk diffusivity as a harmonic average (as appropriate for an average of rates) in the undamaged and damaged portions of the grain. In detail, if the grain had a heterogeneous spatial distribution of U and Th, increasing damage could conceivably produce an apparent spectrum of diffusion domain sizes that might manifest itself in step-heating data as decreasing diffusivity or concave-up Arrhenius trends.

We first parameterize our effective diffusivity using an harmonic average and to do this, we recast equation (1) as:

$$\frac{1}{D_e} = \frac{f'_c}{\left(\frac{1}{-*D_z}\right)} + \frac{f'_a}{D_{N17}} \tag{5}$$

where D_{N17} corresponds to the diffusivity of amorphous N17, and f'_c represents fraction crystalline and is equal to $1 - f'_a$. We again use the direct impact model to describe f'_a and f'_c, but to improve the fit to our diffusion data we include an additional term (ϕ) within the exponential:

$$f'_a = 1 - \exp(-B_a \alpha \phi). \tag{6}$$

A value greater than 1 for ϕ causes f'_a to increase more rapidly at lower alpha doses. As we demonstrate below, a value of 3 for ϕ is necessary for a proper fit to the data, however, we currently have no physical explanation for why this term should be required. It is possible that, while the direct impact model may adequately describe the buildup of amorphous zones in zircon, it does not fully account for the interconnection of certain parts of the zones (for example high-vacancy damage core vs. damage rim), or for the contribution of an additional interacting effect such as accumulation of fission tracks (Ketcham and others, 2013).

In order to account for the reduction of the domain size of the undamaged portion of the grain, we modify equation (5) by dividing each D by domain size (a):

$$\frac{1}{\frac{D_e}{a^2}} = \frac{f'_c}{\frac{1}{\tau} * \left(\frac{D_z}{(a*f'_c)^2}\right)} + \frac{f'_a}{\frac{D_{N17}}{(a*f'_a)^2}}. \quad (7)$$

In this set-up, a is equal to the initial grain size in an undamaged zircon, which effectively decreases as f'_a increases following equation (6).

The ϕ term in equation (6) and the scaling of domain size with f'_a in equation (7) are admittedly somewhat empirical and heuristic, respectively, and their relationship to actual physical phenomena are tenuous. Recent work by Ketcham and others (2013) may offer some additional insight into this issue. These authors suggest that fission track interconnection may play an important, but until recently, underappreciated role in creating the macroscopic and long-range order qualities typically attributed to f_a. Furthermore, they derive an equation for a term that seems to more accurately reflect the effects of radiation damage on decreasing effective domain size: mean distance to nearest fission track d_n. This number decreases with increasing fission track percolation and replacing $(a*f'_c)^2$ with d_n in equation (7) results in a similar functional shape. Unfortunately, doing so does not provide a better fit to the real data. The current calculations do not account for whether the nearest fission track is part of a network connected to the outside of the grain, and improving the model in this respect may result in a better fit. For our present discussion, though, we proceed with equation (7) as it is currently derived.

Our combined equation for effective diffusivity is:

$$\frac{1}{\frac{D_e}{a^2}} = \frac{f'_c}{\frac{1}{\left(\frac{l_{int\,0}}{l_{int}}\right)^2} * \left(\frac{D_z}{(a*f'_c)^2}\right)} + \frac{f'_a}{\frac{D_{N17}}{(a*f'_a)^2}} \quad (8)$$

where $l_{int\,0}$ is equal to 45920 nm (the value of l_{int} calculated from equation (3) at an alpha dose of 1×10^{14} α/g). Figure 10A shows equation (8) with our step-heating results. Our parameterization adequately captures the decrease in diffusivity by ~3 orders of magnitude at low damage and the subsequent increase in diffusivity by ~11 orders of magnitude at high damage. We also show a comparison between the T_c data from figure 8 and T_c values calculated using equation (8) and an initial grain radius of 60 microns (fig. 10B). To obtain effective E_a and D_0 values for this curve, we use a method that relies on pseudo-Arrhenius trends calculated at discrete doses with equation (8). These trends provide the kinetic parameters necessary to then calculate the T_c at the corresponding dose.

Although diffusional anisotropy may manifest itself in our model through the importance of increasing tortuosity at low damage, our model does not directly account for anisotropic diffusion. As figure 6 suggests, the effect of anisotropy on He diffusivity is minimal compared to the effect of radiation damage and we have not focused on it in this section. However, our derivation makes several predictions for a relationship between anisotropy and radiation damage. With increasing damage, c-axis parallel channels might be expected to become increasingly blocked and, correspondingly, anisotropy should decrease (Farley, 2007). Specifically, Mud Tank—our least damaged, oriented zircon—should be more anisotropic than all other samples. Figure 5 shows a large disparity between the D_0 values for the two Mud Tank slabs, and the two trends (constant for PAR_C slabs, decreasing for ORT_C slabs) seem to converge at sample M127. This suggests that, at least in terms of D_0, anisotropic differences decrease with increasing damage. However, the results in figure 6 complicate this observation. At high temperatures (500 °C), the difference in diffusivity between the

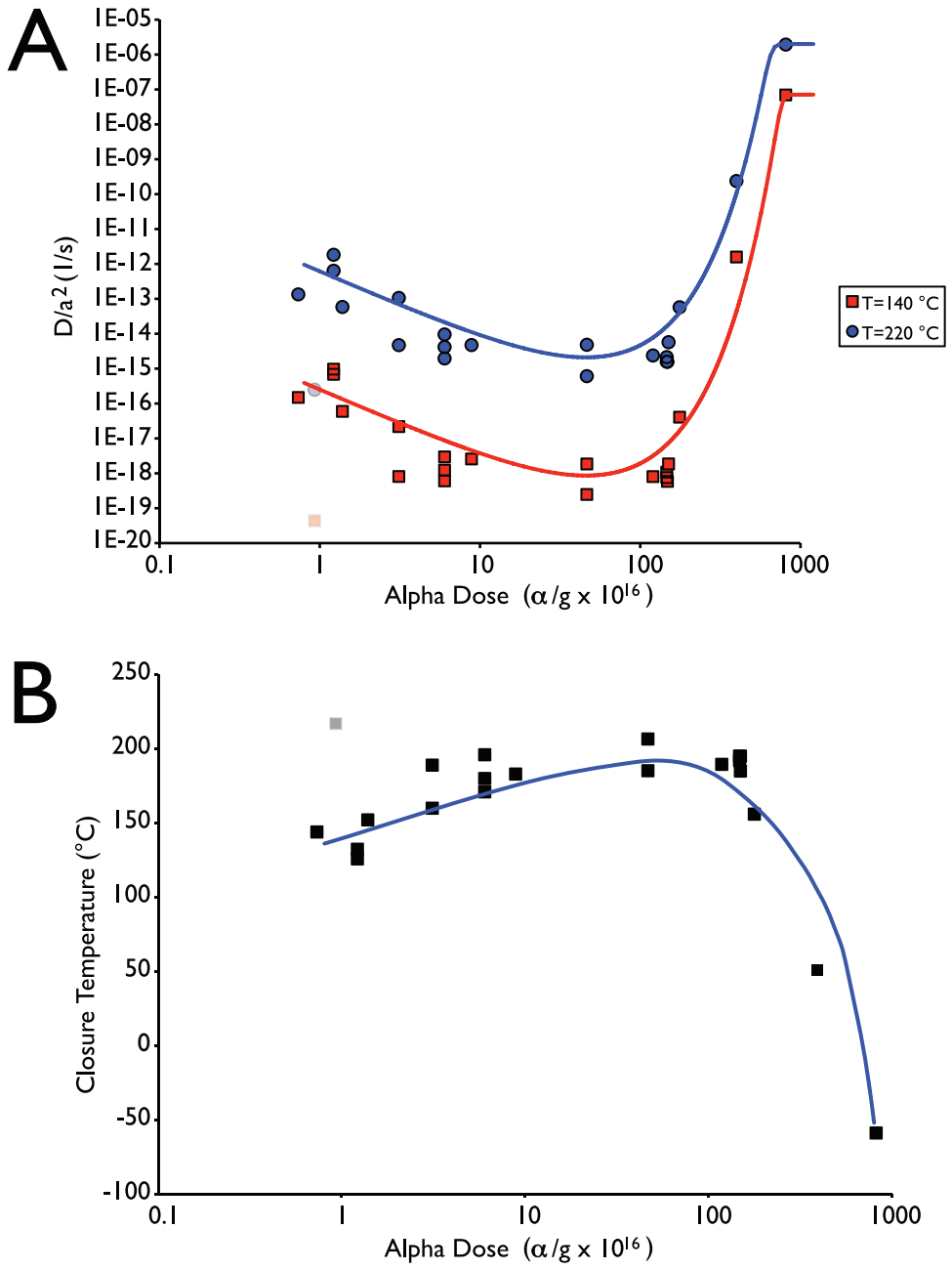

Fig. 10. (A) Diffusivity as a function of alpha dose calculated at temperatures that roughly bracket the nominal zircon PRZ. Data points are the diffusivities of the various samples included in figure 7 (calculated with a domain size of 100 microns) and curves represent effective diffusivity as defined by equation (8). The various parameters used for this plot and their values are listed in table 5. (B) Closure temperature as a function of alpha dose calculated in a manner similar to figure 8. Gray points in both plots represent single sample that does not fall along our observed trend.

Mud Tank slabs is ~2 orders of magnitude, but at lower temperatures the degree of anisotropy between these two slabs is comparable to the anisotropy between slabs in the "moderate to high damage" group (~1 order of magnitude difference, note that the Mud Tank lines have different slopes in figure 6). This suggests that anisotropy is relatively invariant across the damage spectrum from Mud Tank to M127, which seems to contradict our hypothesis that damage decreases the degree of anisotropy. Perhaps the anisotropy in Mud Tank is similar to the anisotropy in M127 because Mud Tank has a large number of other defects that also contribute to decreasing anisotropy. But why then would these defects not also lower diffusivity? We do not have a satisfactory answer for this yet, but point defects may have a relatively small effect on diffusivity compared to radiation damage, due to damage's more chaotic nature. Actual characterization of this difference requires more work. For now we focus our remaining discussion on using equation (8) to forward model date-eU correlations.

Implementation of Damage-Diffusivity Parameterization

As a demonstration of the utility of our parameterization, we link equation (8) to another equation describing damage annealing in zircon and forward model date-eU correlations in a manner similar to the RDAAM (Flowers and others, 2009). Model inputs consist of an effective diffusion domain lengthscale (assumed to be radius of a sphere with an equivalent surface-area to volume ratio as the grain), and U and Th concentrations for each grain, and a discretized t-T history for the entire dataset. With these, our model calculates the total He production, damage accumulation, damage annealing, He diffusivity, and He loss at each time step.

Damage accumulation and annealing are quantified with a series of equations similar to those described by Flowers and others (2009), and rely upon the kinetics of fission track annealing in zircon. Although we treat alpha damage as the primary factor in creating tortuosity and interconnections, using a fission track annealing model means we must assume that alpha damage anneals in a fashion similar to fission tracks. This is a potential problem in the apatite system as well, but the RDAAM's ability to predict date-eU correlations from reasonable t-T histories (for example, Flowers and others, 2007; Flowers and Kelley, 2011) shows that, to first order, modeling damage annealing with fission track kinetics is valid. What works well in apatite, though, may not be suitable for zircon. Especially problematic is the well-documented observation that alpha damage annealing in zircon occurs via two disparate processes—epitaxial recrystallization and ZrO_2 nano-crystal formation—at different temperatures and at different initial damage concentrations (Meldrum and others, 1998; Capitani and others, 2000; Zhang and others, 2000; Nasdala and others, 2002; Zhang and others, 2010). Furthermore, Garver and others (2005) suggested that zircon fission track annealing processes are most likely damage-dependent as well. A possible solution would be to use an alpha damage annealing model that accounts for multiple annealing processes, but despite an extensive literature on alpha damage accumulation and annealing in zircon, to the best of our knowledge, no kinetic model has been parameterized to describe alpha damage annealing at time scales beyond hours or days. If such a model is developed, equation (8) could be easily coupled to it due to our modular model design. More importantly, our main objective here is not to contrast and compare various annealing models. Rather, we simply desire a quantitative approximation of damage annealing kinetics in zircon that seems reasonable for geologic time scales. Given the currently available annealing models, a fission track model best satisfies this requirement.

In order to combine the total alpha damage produced during a series of discrete time steps with a fission track annealing model, we introduce α_e or equivalent alpha dose (α/g):

$$\alpha_e = 6.022 \times 10^{14} \sum_i \alpha_i \rho_{r,i} \tag{9}$$

where the initial factor serves to convert from nmol to decays, α is the number of alpha decays (in nmol) per gram produced in each time step, and ρ_r is reduced (normalized) fission-track density of fission tracks that formed during that time step. The alpha dose from each time step (t_2, t_1) is calculated as:

$$\alpha_i = 8[^{238}U](e^{\lambda_{238}t_2} - e^{\lambda_{238}t_1}) + 7[^{235}U](e^{\lambda_{235}t_2} - e^{\lambda_{235}t_1}) + 6[^{232}Th](e^{\lambda_{232}t_2} - e^{\lambda_{232}t_1}) \tag{10}$$

where $[^{238}U]$, *et cetera* are in nmol/g. Our derivation of ρ_r starts with length reduction r, for which we use a simplified version of the fanning curvilinear fit (for example, Ketcham and others, 2007) to the ZFT annealing data of Yamada and others (2007):

$$r = \frac{l}{l_0} = \left[\left(C_0 + C_1 \frac{\ln(t) - C_2}{\ln(1/T) - C_3} \right)^{1/\beta} + 1 \right]^{-1} \tag{11}$$

where $\beta = -0.05721$, $C_0 = 6.24534$, $C_1 = -0.11977$, $C_2 = -314.937$, and $C_3 = -14.2868$. To convert from reduced length to reduced density (ρ_r), we use the relation based on data reported by Tagami and others (1990), which begins at one and is truncated at a ρ/ρ_0 value of 0.36, below which there are no data:

$$\rho_r = \frac{\rho}{\rho_0} = 1.25(r - 0.2). \tag{12}$$

Once calculated, values of α_e are linked to a diffusion model via equation (8). With an estimate of the diffusion coefficient from equation (8), we then solve the diffusion equation numerically for a spherical geometry with the Crank-Nicholson finite difference scheme used in the thermal modeling software package HeFTy (Ketcham, 2005). Although this is not the best representation of He diffusion in zircon (it implies isotropic diffusion), a spherical model captures the first-order features of the damage-diffusivity relationship. Future versions could incorporate the cylindrical finite element scheme of Watson and others (2010), which accounts for the effects of anisotropy. Alternatively, a spherical calculation scheme can be employed using the "active radius" method introduced by Gautheron and Tassan-Got (2010), who described how to determine the radius of an isotropic sphere that replicates diffusive loss from a prism with a given aspect ratio and diffusive anisotropy.

Our model demonstration consists of 6 different thermal histories, each designed to capture aspects of the date-eU correlations in figures 1 and 2. As inputs, we use eU ranging from ~50 to ~5000 ppm, grain radii of 60 μm, and *t-T* paths that begin at 600 Ma and end at the present. For comparison, we also model the single zircon He date that results from using the kinetics of Reiners and others (2004) with each of our thermal histories (black diamonds in fig. 11B). These *t-T* paths encapsulate 6 representative scenarios: 1) slow, monotonic cooling from 600 Ma to the present, 2) early cooling followed by a pulse of early-stage reheating, 3) early cooling followed by a pulse of late-stage reheating, 4) early cooling followed by prolonged time spent in the PRZ and then subsequent late cooling, 5) long term early heating and subsequent late-stage cooling, and 6) early cooling and prolonged exposure to low temperatures (fig. 11). Model outputs that result from scenarios 5 and 6 show mostly flat date-eU correlation, which are typical of most zircon He datasets. These two scenarios also result in He dates that are almost identical to dates obtained using the kinetics of Reiners and others (2004). For thermal histories with a single, rapid pulse of cooling from high temperatures, our new model does not alter interpretations of zircon He datasets made with previously published kinetics as this style of cooling will most likely not result in a

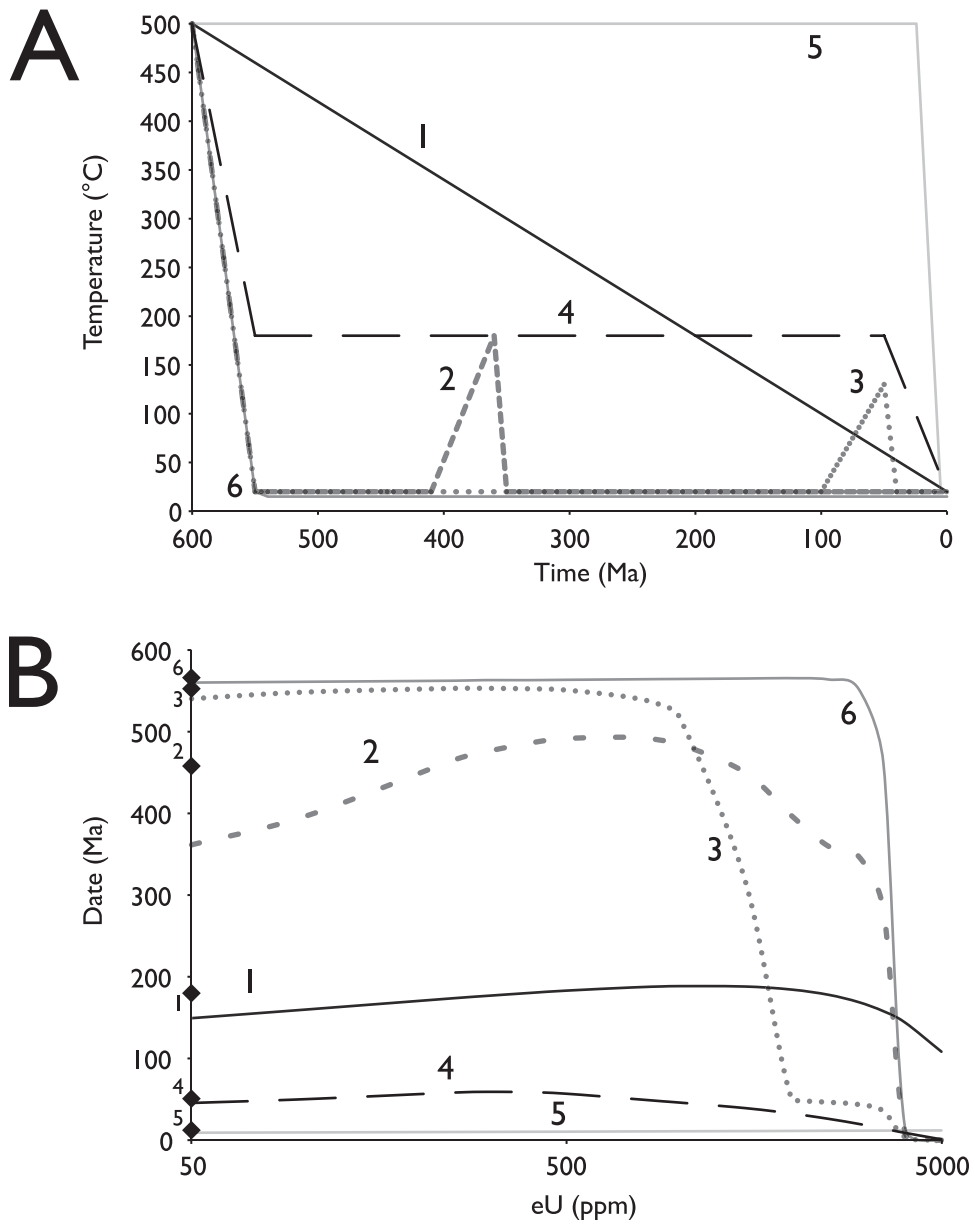

Fig. 11. Representative thermal histories (A) with corresponding forward modeled date-eU correlations (B). Each numbered *t-T* path in (A) corresponds to the similarly numbered correlation in (B). Thermal history number 6 is partially obscured by 2 and 3 because it follows the same path but lacks a post-500 Ma reheating event. For reference, we also plot the zircon He dates that result from each thermal history in (A) if the kinetics of Reiners and others (2004) are used. These are represented by the numbered black diamonds on the y-axis of (B).

date-eU correlation. Interestingly though, scenario 6 shows a steep negative correlation at high damage, despite having never been reheated above 20 °C post-500 Ma. These zircons have entered the PRZ without changing temperature and we note that a similar process may have occurred in the Sri Lankan dataset to produce the young dates for zircons K6 and N17.

Scenarios 1, 2, 3, and 4 demonstrate the various thermal histories that may produce positive, negative, or both types of correlations in the same sample. The thermal history for scenario 1 is characterized by slow cooling through the PRZ and results in a broad and relatively confined positive date-eU correlation (dates increase from 161-210 Ma). Damage in-growth and He diffusion occur simultaneously over a prolonged time span, which causes the damage amounts for the zircons in this scenario to be relatively similar while He is diffusing. Given high enough eU concentrations, the *t-T* path for scenario 1 also produces negative correlations in the same sample. Although this particular negative correlation is subtle, an older initial age for the start of slow cooling could produce a more pronounced negative correlation, as we further demonstrate with our Minnesota dataset below. Scenario 4 is somewhat similar to scenario 1 as both samples spend prolonged time periods in the PRZ. However, for most of their history, the zircons in scenario 4 are held at a lower temperature (180 °C) than those in scenario 1. At this temperature, damage in-growth outpaces annealing and the thermal history produces a negative correlation at relatively low eU concentrations once the sample is finally cooled.

In contrast, relatively short-lived pulses of reheating and cooling result in more marked positive or negative correlations. The thermal histories for both scenarios 2 and 3 contain reheating events that take place after the zircons have been held at low temperatures (20 °C) for at least 100 my. During this time span, the zircons in each scenario have acquired large differences in damage. In scenario 2, this results in a positive correlation that spans a date range from 428 to 538 Ma, but also a negative correlation that drops to zero at the highest eU. Like scenario 6, the PRZ for zircons with eU in excess of ~3500 ppm is at very low temperatures and they no longer retain He. In scenario 3, we have chosen both a later start time (100 Ma) and a lower maximum temperature for the reheating event than scenario 2 (130 °C as opposed to 180 °C). The resulting plateau of dates at ~550 Ma followed by a steep negative correlation is somewhat similar to scenario 6, except the steep drop off in dates occurs over much lower eU concentrations (from ~1500 to 2000 ppm). The late-stage reheating event also produces a small plateau of ~50 Ma dates at eU concentrations greater than ~2000 ppm. These dates correspond to the initiation of cooling and illustrate that, given a large span in radiation damage, multiple pulses of reheating and subsequent cooling could be recorded in zircons from the same hand sample.

As a final demonstration, we forward model the thermal history of two real datasets shown in figures 1 and 2. We use one of the Apennines datasets (AP54B) as a representative positive date-eU correlation, and the Minnesota dataset as a representative negative date-eU correlation. For each dataset, we present a realistic thermal history that could have produced the observed data and show the resulting model output in figure 12. In the Apennines example, we rely on the thermochronometric data from previous publications to guide our *t-T* path construction. Bernet and others (2001) obtained ZFT dates on the same grains shown in figures 1 and 12A, which yield a peak date of 20.7±3.6 Ma (these author's P1 population). This translates to a lag time of 6.8 my as the depositional age of this particular unit in the Marnoso-arenacea Formation is 13.9 Ma. Zattin and others (2002) conducted a detailed regional study of this Formation and found that fully and partially reset AFT dates from their hinterland samples (most internal to the thrust belt) suggest maximum burial temperatures of 120 to 125 °C and post-depositional exhumation between 4 and 6 Ma. If we consider these multiple *t-T* constraints as model inputs, then we can produce the black line in figure 12A, a positive date-eU correlation that is in good agreement with the real dataset. In figure 12A, we also show the results from a simpler thermal history (dotted lines in *t-T* history and date-eU correlation) in order to demonstrate that our preferred thermal history (black line) produces a distinctive date-eU trend that best fits the data.

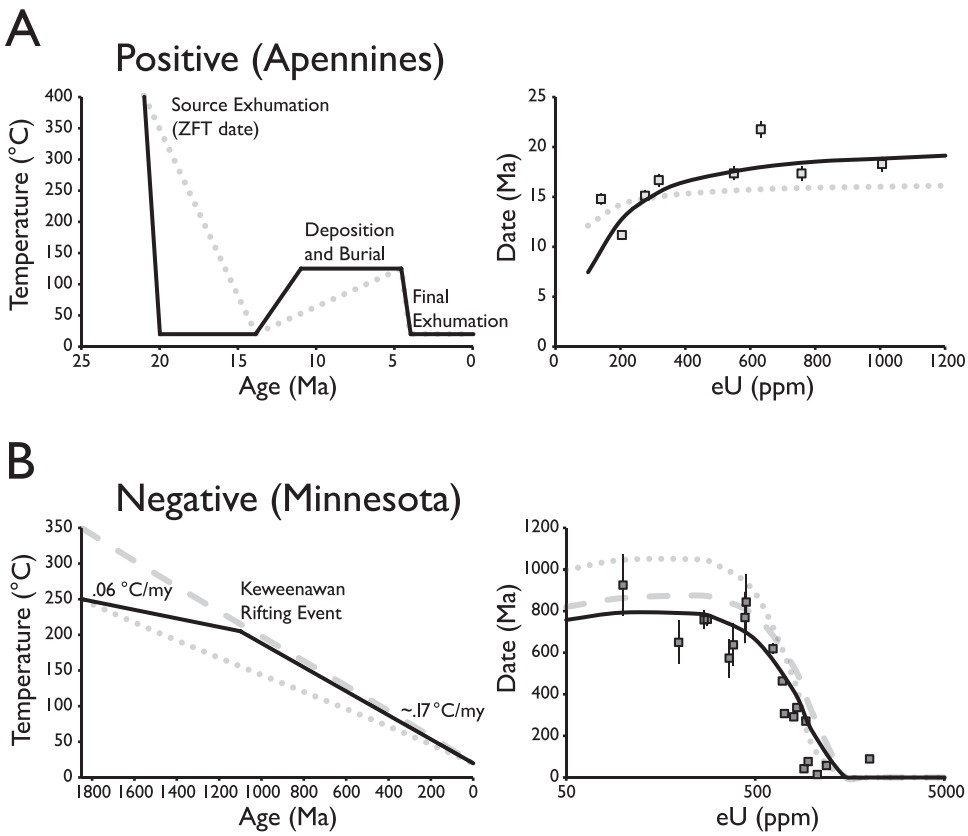

Fig. 12. Forward modeled date-eU correlations matched to datasets shown in figures 1 and 2. (A) Positive date-eU correlation (detrital Apennines sample AP54B) with forward modeled correlation resulting from thermal history shown in the left-hand panel. This thermal history is characterized by a period of rapid exhumation in the source terrain (as constrained by ZFT dates from Bernet and others, 2001), deposition and burial in the Apennine foreland basin, and final exhumation to the surface in the latest Miocene. We used a grain radius of 48 microns for each model zircon, which is the average for this dataset. Dotted light gray lines in both panels represent an alternative thermal history and the corresponding date-eU correlation. (B) Negative date-eU correlation (igneous Minnesota River Valley sample) with forward model correlation resulting from the thermal history shown in the left-hand panel. This thermal history begins at the approximate end of tectonism associated with the Penokean Orogeny in this area and proceeds at a cooling rate of .06 °C/my until 1100 Ma. This time corresponds with the initiation of the Keweenaw Rift System (the Minnesota River Valley was situated near the rift shoulder) and we model this as an increase in the long-term cooling rate to ~.17 °C/my. Again, we used the average grain radius from this dataset (52 microns) as an input for each model zircon. Dashed and dotted lines in both panels represent two alternative thermal histories and the corresponding date-eU correlations.

Our new model therefore tightly constrains the thermal history of a given sample and discriminates between potential *t-T* paths.

Our Minnesota dataset has fewer *t-T* constraints and our modeled *t-T* path is slightly more speculative. A negative date-eU correlation and an oldest date of ~925 Ma though suggests that these zircons have experienced very slow cooling rates since the Proterozoic. With this in mind, we explored several possible slow cooling paths since the Penokean orogeny at 1870 to 1820 Ma, which is the most recent episode of regional metamorphism to affect this area (Holm and others, 1998). Our best fit to the data consists of an initial cooling event beginning at 1850 Ma and 250 °C that proceeds at a rate of .06 °C/my. In order to reproduce both the pseudo-plateau of dates at low

eU concentrations and the steep negative correlation at high eU concentrations, we accelerate our cooling rate from .06 °C/my to ~.17 °C/my at 1100 Ma, which matches the age of opening for the failed Keweenawan Rift system. Again, we include the results from a couple of simpler histories (dotted and dashed lines in fig. 12B) to show that our choice for the Minnesota thermal history is not arbitrary. Slow cooling rates with a single value yield date-eU correlations that match either the high eU or low eU trends in the real data, but not both. We find a good fit to the data only by changing the cooling rate at a specific time (in this case, 1100 Ma). Despite being somewhat speculative, our model *t-T* constraints for the Minnesota dataset agree with the regional geologic history, produce a reasonable fit to the data, and demonstrate that the Minnesota sample has experienced very slow cooling at low temperatures for the past 1.8 by.

Impact of eU Zonation on Zircon Date-eU Correlations

In the above models, we assumed that both our real and model zircons are homogenous in their U and Th (hence eU) concentrations. Typical zircons, though, usually possess some degree of U and Th zonation. Although previous studies have discussed the effects of parent zonation on apatite (U-Th)/He dates in depth (for example, Farley and others, 1996; Meesters and Dunai, 2002; Hourigan and others, 2005; Farley and others, 2011; Ault and Flowers, 2012; Gautheron and others, 2012), the effects of strong parent zonation in zircon may be significantly different because of the reversal in damage-diffusivity relationship with progressive damage accumulation. This means that, for some thermal histories, different parts of the same zircon grain may have extremely different behavior, both of which may be very different from that expected from a grain with equivalent bulk eU homogeneously distributed.

Farley and others (2011) detailed three ways in which heterogeneous eU in zoned apatite (lacking the damage-diffusivity reversal potential) can affect measured ages and interpreted t-T histories. If an homogenous alpha ejection correction factor (F_{TH}) is used for a zoned grain, then the resulting He date will be either too young or too old depending on where the majority of eU is concentrated (rim or core, respectively) (Farley and others, 1996; Hourigan and others, 2005). This issue can be dealt with by using a zoned alpha ejection correction (F_{TZ}) that accounts for alpha particle redistribution, which is an option in HeFTy. Zonation also affects He diffusivity by altering the He concentration profile, and, because He diffusion is damage dependent, by creating distinct domains with different diffusion kinetics inside the crystal. In the apatite He system, these three factors can contribute to He date scatter (Flowers and Kelley, 2011). Ault and Flowers (2012) suggested, however, that for typical apatites eU concentrations between zones do not vary by more than a factor of ~2, and for typical thermal histories the resulting relative date difference between zoned and homogenous apatites with the same bulk eU is no more than ~10 percent.

We expect these zonation issues to result in greater fractional date differences for the zircon He system. Order of magnitude differences in eU zonation are not uncommon in zircons (for example, fig. 13 in Reiners and others, 2004), and these can cause large discrepancies in both damage and He concentration. Furthermore, unlike apatite, He diffusivity in zircon will either decrease or increase depending on the eU concentration of a given zone and the specific *t-T* path of the zircon. The interplay amongst the alpha ejection correction factors, He concentration profiles, and damage profiles in zoned zircons with different thermal histories is therefore complicated and a detailed examination of real He datasets with zoned grains is beyond the scope of our current study. However, we discuss below the results from several HeFTy models to show how zonation affects differential damage accumulation within a zircon and sample date-eU correlations.

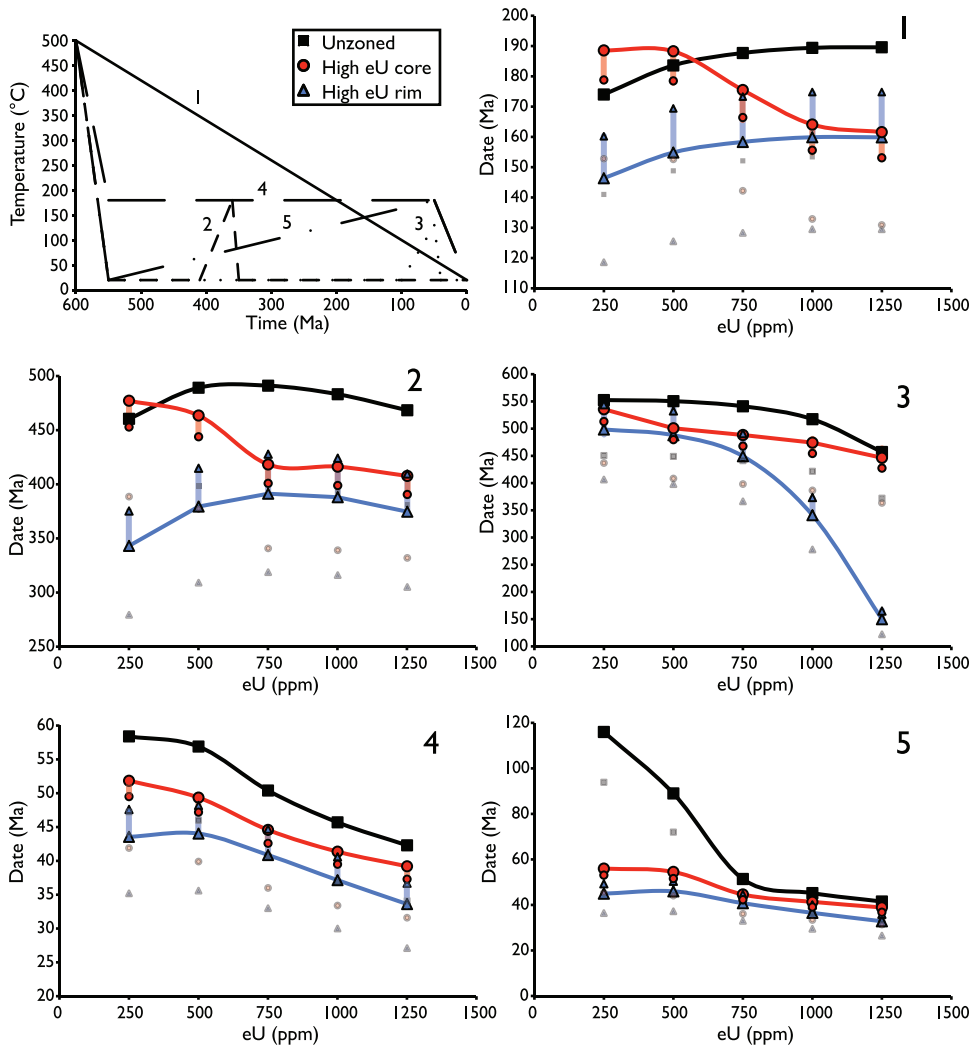

Fig. 13. Time-temperature histories and corresponding date-eU correlations for unzoned zircons, zircons with high eU rims, and zircons with high eU cores. The numbering for each *t-T* path is similar to figure 11, except we have omitted number 6 and replaced number 5 with a different thermal history. Core eU concentrations are either enriched or depleted by a factor of 7 relative to the bulk concentration of the whole grain. For example, if the bulk concentration is 500 ppm, then the core concentration in the high eU core zircon is 3500 ppm and it is ~71 ppm in the high eU rim zircon. Both the concentration in the rim and the radial position of the rim are determined by maximizing the zircon zonation factor (see text for details). All zircons have a radius of 60 microns and the core is composed of either the inner 20 or 40 microns of the grain. Large bold symbols connected by horizontal curves represent F_{TH} corrected dates, small bold symbols represent F_{TZ} corrected dates, and small transparent symbols represent uncorrected dates. Lightly colored vertical bars have been added to aid in connecting corresponding F_{TH} and F_{TZ} corrected dates. See text for details on uncorrected, F_{TH}, and F_{TZ} corrected zircons. Note that the scale for each y-axis is different.

These model simulations consist of five representative thermal histories and the resulting date-eU correlations for a suite of unzoned zircons and zircons with simple concentric zonation of high eU cores or high eU rims (fig. 13). Both the zoned and unzoned zircons in each plot have bulk eU concentrations ranging from 250 to 1250 ppm with radii of 60 microns. The zonation profiles for the zircons in our models have

two main inputs, the core eU concentration and the core's radial position (rim concentration is set by the bulk eU). In order to provide some uniformity to our choice of variables, we use a zonation impact index (mass of eU for the whole grain divided by the mass difference between the core and rim), which provides a rough estimate of magnitude of the effect that eU zonation has on a zircon's He concentration and damage profile. For a given bulk and core eU concentration, this value reaches a maximum at a certain core radial position and rim eU concentration. In turn, this particular radial position and rim eU maximizes the difference in diffusion kinetics between rim and core that result from He concentration and radiation damage disparities. Because we want to show a worst-case scenario for each date-eU correlation, we have chosen the rim eU concentration and core radial position that correspond to the maximum zonation impact number. For core eU concentration, we pick values that differ from the bulk eU concentration by a factor of seven (a bulk eU of 500 ppm leads to a core eU of either 71.4 or 3500 ppm), which results in a core radial position that is 20 microns from the center (total radius of 60 microns) for the enriched core zircons, and a core radial position that is 40 microns from the center for the enriched rim zircons. In zircons with enriched rims, the ratio between eU concentrations in the rim and core is 9.52:1, while the same ratio is 1:9.1 for zircons with enriched cores. A final consideration is the choice of a F_{TH} or a F_{TZ} alpha ejection correction. For unzoned zircons, we model both the uncorrected date at a given eU and the F_{TH} corrected date ($F_{TH} = F_{TZ}$ for the unzoned case). For each zoned zircon, we model the uncorrected date, the F_{TZ} corrected date using the "redistribution" option in HeFTy, and the F_{TH} corrected date. The F_{TH} for each zoned zircon is calculated by taking the ratio between the unzoned F_{TH} corrected date at equivalent eU and the unzoned uncorrected date at equivalent eU. For zoned grains, the F_{TH} date is equivalent to measuring a raw grain date on a zoned zircon and applying a naive alpha ejection correction assuming no parent zonation.

The model results for all corrected and uncorrected zircons are shown in figure 13. Thermal histories 1 through 4 are the same as in figure 11. We have omitted *t-T* paths 5 and 6 from figure 11 as both of these yield nearly flat date-eU correlations for zoned and unzoned zircons. Instead, we have added a new *t-T* path 5 to figure 13 that could be appropriate for zircons from Laramide uplifts of the US Rocky Mountains (for example, our Bighorn sample). In all *t-T* scenarios, the F_{TH} corrected zoned dates (large bold symbols connected by curves in fig. 13) for zircons with high eU rims are younger than their unzoned counterparts. Only some of this discrepancy is due to an improper alpha ejection correction, as the F_{TZ} corrected zoned dates (small bold symbols) are also younger than unzoned zircons with the same bulk eU. The other causes for younger dates—which in scenarios 3, 4 and 5, are the predominant ones—are the combined effects of a heterogeneous He concentration profile and radiation damage. Rims that are enriched in eU relative to the core cause an increase in effective bulk diffusivity (and younger dates) because more He is located near the grain boundary, and, at high eU concentrations, the rims become heavily damaged. This damage effect is particularly apparent in scenario 3, where the grains with the highest bulk eU concentrations have accumulated enough damage such that the rim acts as a diffusion fast path. If we model the high-eU-rim zircon with a bulk eU of 1250 ppm using the kinetics of Reiners and others (2004), then this scenario yields a date of 544 Ma (as opposed to 256 Ma using the kinetics presented here), which further suggests that radiation damage is the primary cause of these younger dates.

Despite being systematically younger, most of the high-eU-rim dates have a similar style of date-eU correlation as the unzoned dates. One exception is scenario 5, where a date-eU correlation that is monotonically negative in the unzoned case is positive at low bulk eU concentrations. Although the rims of the high-eU-rim

zircons have accumulated high degrees of damage prior to cooling, the cores range from low ($\sim 5.5 \times 10^{16}$ α/g at 50 Ma) to moderate ($\sim 1.1 \times 10^{17}$ α/g at 50 Ma) amounts of damage. This difference in damage is enough to cause a more retentive core and lower bulk diffusivity in the 500 ppm bulk eU grain than the 250 ppm bulk eU grain, which in turn results in a positive date-eU correlation over this eU range.

To explain the date-eU correlations for the high-eU-core zircons, we must similarly consider the degree of damage in both the core and the rim and how those two damage domains combine to affect bulk diffusivity. In scenario 1, dates are either older or younger than the unzoned dates at the same eU, and the style of date-eU correlation changes from a positive correlation in the unzoned grains to a positive-negative-plateau correlation in the high-eU-core grains. The onset of a negative correlation has shifted as the zircon core accumulates a high degree of damage (and therefore has a high diffusivity) at relatively low bulk eU concentrations. Interestingly though, a plateau at the highest bulk eU concentrations suggests that the high diffusivity of the core is somewhat mitigated by the degree of damage in the zircon's rim. A similar phenomenon occurs in scenario 2, and is especially apparent in scenario 3 if we compare the high-eU-rim grains with the high-eU-core grains. In scenarios 1 and 2, the rims of the high-eU-core zircons at high bulk eU concentrations have accumulated a moderate amount of damage (roughly 4×10^{17} α/g prior to any thermal event) such that the rim decreases diffusivity and acts to retard He diffusing out of the crystal, similar to the effects of RDAAM on zoned apatites with eU enriched rims (Farley and others, 2011; Ault and Flowers, 2012). For the rims of the high-eU-core grains in scenario 3, the damage accumulation is more substantial, but the final reheating event occurs at a relatively low temperature. This temperature is low enough to cause these zircon rims to be more retentive than the corresponding rims in the high-eU-rim zircons (and thus yield older dates).

In contrast to scenarios 1, 2, and 3, the thermal histories in 4 and 5 result in damage higher than $\sim 5 \times 10^{17}$ α/g, and relatively high diffusivity in both the cores and rims for most bulk eU concentrations. In terms of damage, this places almost all of the domains in these high-eU-core zircons to the high-damage side of the point of lowest diffusivity in figure 10A. The rims of the high-eU-core zircons with 250 ppm bulk eU concentrations are the only domains with damage lower than 5×10^{17} α/g (both are $\sim 3 \times 10^{17}$ α/g prior to final cooling at 50 Ma) in these two scenarios. The net result in both scenarios is a date-eU correlation for the high-eU-core grains that is similar in style to the unzoned zircons, but with systematically younger dates. An exception to this is the positive correlation for bulk eU concentrations of 250 ppm and 500 ppm in scenario 5. Among the high-eU-core grains, the rim for the 250 ppm bulk eU grain has a damage amount of $\sim 2.9 \times 10^{17}$ α/g at 50 Ma (the age prior to final cooling), while the rim for the 500 ppm bulk eU grain has a damage amount of $\sim 5.8 \times 10^{17}$ α/g at 50 Ma. This difference in damage causes the 500 ppm bulk eU grain to have a more retentive rim and thus lower bulk diffusivity relative to the 250 ppm bulk eU grain, which in turn produces a slight positive correlation.

These five *t-T* scenarios illustrate that date-eU correlations for zoned zircons may be complex because of reasons already discussed in previous studies, but also because of the reversal in He diffusion behavior with progressive damage accumulation. In the absence of *a priori* knowledge of parent zonation patterns, the effects of parent zonation on He diffusivity may complicate thermochronologic interpretations of date-eU correlations. We again note that we have purposely chosen worst-case zoning scenarios in order to convey the full scope of this issue. Real zircons may possess a less extreme degree or pattern of zonation, which will mitigate some of the date dispersion observed in figure 13. Consistent styles but variable degrees of zonation (for example, enriched rim but with varying rim thickness or enrichment factor relative to the core)

may be expected among zircons from some rock types. This would produce dispersion in a band of date-eU correlations between the unzoned case (black curves) and an extreme zoned case (blue or red curves, depending on zonation style) in figure 13. However, suites of zircons from some samples may not possess systematic zonation patterns like those in figure 13. Especially in detrital settings, one may expect to date zircons with a range of zonation patterns: some may have high eU cores, some may have high eU rims, and others might be unzoned. In this context, the curves in figure 13 should be interpreted as bounding constraints for the total range of zonation variability. For a given *t-T* path, and no consistent zonation style, real date-eU correlations could potentially plot anywhere within the black, blue, or red curves.

Despite the apparent severity of the zonation problem, however, parent zonation may be characterized from laser ablation depth profiles or other techniques, prior to bulk grain dating. These observations also point to the potential for exploiting parent zonation to provide date-eU trends within individual grains, for example with *in-situ* laser ablation dating (Vermeesch and others, 2012). Under certain conditions, zircon grains with zoned parent concentrations may behave similarly to crystals with multiple He diffusion domains. *In-situ* measurements and/or step-heating analyses could potentially be used to interrogate the distribution of He and dates among these domains, providing powerful constraints on thermal histories from single grains.

CONCLUSIONS

Several suites of single-grain zircon (U-Th)/He dates from single rock samples show positive and negative correlations with eU. These correlations are a consequence of the two different ways that radiation damage affects He diffusion in zircon. Evidence for two contrasting effects of radiation damage (as related to alpha dose) on diffusion comes from zircon step-heating experiments, which show that between about 1×10^{16} and 5×10^{17} α/g, diffusivity decreases by about three orders of magnitude. Diffusivity then begins to increase rapidly with increasing damage, by up to 10 orders of magnitude at damage levels of sample N17 ($\sim 8 \times 10^{18}$ α/g). We hypothesize that decreases in diffusivity at low damage are caused by damage zones blocking preferred c-axis parallel pathways. As damage levels approach N17, these zones become increasingly interconnected and form through-going fast diffusion pathways that shrink the effective diffusion domain size. We parameterize the damage-diffusivity relationship with an equation that combines both of these effects. We also couple our parameterization to an equation for damage annealing in order to forward model date-eU correlations from specific *t-T* histories. Our model offers insight into some of the issues associated with He diffusion in natural zircons and provides other researchers with a tool for understanding and exploiting the significance of date dispersion in zircon He datasets.

ACKNOWLEDGMENTS

This work was supported by NSF grant EAR-0910577 to PWR as well as funding from the COSA2 Collaboration between UA Geosciences and ExxonMobil. L.N. acknowledges financial support by the Austrian Science Fund (FWF) through grants P20028-N10 and P24448-N19. Jiba Ganguly and Sumit Chakraborty provided helpful comments on some of the equations. Sri Lankan reference zircon samples were kindly made available by Allen K. Kennedy (RB140, BR231, G3) and Wolfgang Hofmeister (M127, N17). We are grateful to Andreas Wagner for the preparation of the doubly polished slabs, and to Uttam Chowdhury for analytical assistance. We thank Madalyn Blondes and Louise Miltich for allowing us to present some of their previously unpublished zircon He dates from the Apennines and Minnesota, respectively, and we thank Ian Campbell and Charlotte Allen for the Cooma samples. We appreciate helpful reviews by David Shuster, Rebecca Flowers, and Andrew Carter.

References

Ault, A. K., and Flowers, R. M., 2012, Is apatite U-Th zonation information necessary for accurate interpretation of apatite (U-Th)/He thermochronometry data?: Geochimica et Cosmochimica Acta, v. 79, p. 60–78, http://dx.doi.org/10.1016/j.gca.2011.11.037

Bengston, A., Ewing, R. C., and Becker, U., 2012, He diffusion and closure temperatures in apatite and zircon: A density functional theory investigation: Geochimica et Cosmochimica Acta, v. 86, p. 228–238, http://dx.doi.org/10.1016/j.gca.2012.03.004

Bernet, M., Zattin, M., Garver, J. I., Brandon, M. T., and Vance, J. A., 2001, Steady-state exhumation of the European Alps: Geology, v. 29, n. 1, p. 35–38, http://dx.doi.org/10.1130/0091-7613(2001)029⟨0035:SSEOTE⟩2.0.CO;2

Blackburn, T. J., Stockli, D. F., and Walker, J. D., 2007, Magnetite (U-Th)/He dating and its application to the geochronology of intermediate to mafic volcanic rocks: Earth and Planetary Science Letters, v. 259, n. 3–4, p. 360–371, http://dx.doi.org/10.1016/j.epsl.2007.04.044

Capitani, G. C., Leroux, H., Doukhan, J. C., Rios, S., Zhang, M., and Salje, E. K. H., 2000, A TEM investigation of natural metamict zircons: Structure and recovery of amorphous domains: Physics and Chemistry of Minerals, v. 27, n. 8, p. 545–556, http://dx.doi.org/10.1007/s002690000100

Chakraborty, S., 2008, Diffusion in solid silicates: A tool to track timescales of processes comes of age: Annual Review of Earth and Planetary Science, v. 36, p. 153–190, http://dx.doi.org/10.1146/annurev.earth.36.031207.124125

Cherniak, D. J., and Watson, E. B., 2003, Diffusion in zircon *in* Hanchar J. M., and Hoskin, P. W. O., editors, Zircon: Reviews in Mineralogy and Geochemistry, v. 53, p. 113–143, http://dx.doi.org/10.2113/0530113

Cherniak, D. J., Watson, E. B., and Thomas, J. B., 2009, Diffusion of helium in zircon and apatite: Chemical Geology, v. 268, n. 1–2, p. 155–166, http://dx.doi.org/10.1016/j.chemgeo.2009.08.011

Clay, P. L., Baxter, E. F., Cherniak, D. J., Kelley, S. P., Thomas, J. B., and Watson, E. B., 2010, Two diffusion pathways in quartz: A combined UV-laser and RBS study: Geochimica et Cosmochimica Acta, v. 74, n. 20, p. 5906–5925, http://dx.doi.org/10.1016/j.gca.2010.07.014

Cussler, E. L., 1984, Diffusion: Mass transfer in fluid systems: New York, Cambridge University Press, 525 p.

DeCelles, P. G., 1994, Late Cretaceous-Paleocene synorogenic sedimentation and kinematic history of the Sevier thrust belt, northeast Utah and southwest Wyoming: Geological Society of America Bulletin, v. 106, n. 1, p. 32–56, http://dx.doi.org/10.1130/0016-7606(1994)106⟨0032:LCPSSA⟩2.3.CO;2

Devanathan, R., Corrales, L. R., Weber, W. J., Chartier, A., and Meis, C., 2006, Molecular dynamics simulation of energetic uranium recoil damage in zircon: Molecular Simulation, v. 32, n. 12–13, p. 1069–1077, http://dx.doi.org/10.1080/08927020600959929

Dijkman, F. G., and van der Maas, J. H., 1976, Dependence of bandshape and depolarization ratio on slitwidth: Applied Spectroscopy, v. 30, n. 5, p. 545–546, http://dx.doi.org/10.1366/000370276774456859

Epstein, N., 1989, On tortuosity and the tortuosity factor in flow and diffusion through porous media: Chemical Engineering Science, v. 44, n. 3, p. 777–779, http://dx.doi.org/10.1016/0009-2509(89)85053-5

Ewing, R. C., Meldrum, A., Wang, L., Weber, W. J., and Corrales, L. R., 2003, Radiation effects in zircon, *in* Hanchar J. M., and Hoskin, P. W. O., editors, Zircon: Reviews in Mineralogy and Geochemistry, v. 53, p. 387–425, http://dx.doi.org/10.2113/0530387

Farley, K. A., 2000, Helium diffusion from apatite: General behavior as illustrated by Durango fluorapatite: Journal of Geophysical Research—Solid Earth, v. 105, n. B2, p. 2903–2914, http://dx.doi.org/10.1029/1999JB900348

——— 2007, He diffusion systematics in minerals: Evidence from synthetic monazite and zircon structure phosphates: Geochimica et Cosmochimica Acta, v. 71, n. 16, p. 4015–4024, http://dx.doi.org/10.1016/j.gca.2007.05.022

Farley, K. A., Wolf, R. A., and Silver, L. T., 1996, The effects of long alpha-stopping distance on (U-Th)/He ages: Geochimica et Cosmochimica Acta, v. 60, n. 21, p. 4223–4229, http://dx.doi.org/10.1016/S0016-7037(96)00193-7

Farley, K. A., Reiners, P. W., and Nenow, V., 1999, An apparatus for high-precision helium diffusion measurements from minerals: Analytical Chemistry, v. 71, n. 10, p. 2059–2061, http://dx.doi.org/10.1021/ac9813078

Farley, K. A., Shuster, D. L., and Ketcham, R. A., 2011, U and Th zonation in apatite observed by laser ablation ICPMS, and implications for the (U-Th)/He system: Geochimica et Cosmochimica Acta, v. 75, n. 16, p. 4515–4530, http://dx.doi.org/10.1016/j.gca.2011.05.020

Fechtig, H., and Kalbitzer, S., 1966, The diffusion of argon in potassium-bearing solids, *in* Schaeffer, O. A., and Zahringer, J., editors, Potassium Argon Dating: New York, Springer-Verlag, p. 68–107.

Flowers, R. M., and Kelley, S. A., 2011, Interpreting data dispersion and "inverted" dates in apatite (U-Th)/He and fission-track datasets: An example from the US midcontinent: Geochimica et Cosmochimica Acta, v. 75, n. 18, p. 5169–5186, http://dx.doi.org/10.1016/j.gca.2011.06.016

Flowers, R. M., Shuster, D. L., Wernicke, B. P., and Farley, K. A., 2007, Radiation damage control on apatite (U-Th)/He dates from the Grand Canyon region, Colorado Plateau: Geology, v. 35, n. 5, p. 447–450, http://dx.doi.org/10.1130/G23471A.1

Flowers, R. M., Ketcham, R. A., Shuster, D. L., and Farley, K. A., 2009, Apatite (U-Th)/He thermochronometry using a radiation damage accumulation and annealing model: Geochimica et Cosmochimia Acta, v. 73, n. 8, p. 2347–2365, http://dx.doi.org/10.1016/j.gca.2009.01.015

Garver, J. I., Reiners, P. W., Walker, L. J., Ramage, J. M., and Perry, S. E., 2005, Implications for timing of Andean uplift from thermal resetting of radiation-damaged zircon in the Cordillera Huayhuash, northern Peru: The Journal of Geology, v. 113, n. 2, p. 117–138, http://dx.doi.org/10.1086/427664

Gautheron, C., and Tassan-Got, L., 2010, A Monte Carlo approach to diffusion applied to noble gas/helium

thermochronology: Chemical Geology, v. 273, n. 3–4, p. 212–224, http://dx.doi.org/10.1016/j.chemgeo.2010.02.023
Gautheron, C., Tassan-Got, L., Barbarand, J., and Pagel, M., 2009, Effect of alpha-damage annealing on apatite (U-Th)/He thermochronology: Chemical Geology, v. 266, n. 3–4, p. 157–170, http://dx.doi.org/10.1016/j.chemgeo.2009.06.001
Gautheron, C., Tassan-Got, L., Ketcham, R. A., and Dobson, K. J., 2012, Accounting for long alpha-particle stopping distances in (U-Th-Sm)/He geochronology: 3D modeling of diffusion, zoning, implantation, and abrasion: Geochimica et Cosmochimica Acta, v. 96, n. 1, p. 44–56, http://dx.doi.org/10.1016/j.gca.2012.08.016
Gibbons, J. F., 1972, Ion implantation in semicondoctors—Part II: Damage production and annealing: Proceedings of the IEEE, v. 60, n. 9, p. 1062–1096, http://dx.doi.org/10.1109/PROC.1972.8854
Green, P. F., Crowhurst, P. V., Duddy, I. R., Japsen, P., and Holford, S. P., 2006, Conflicting (U-Th)/He and fission track ages in apatite: Enhanced He retention, not anomalous annealing behavior: Earth and Planetary Science Letters, v. 250, n. 3–4, p. 407–427, http://dx.doi.org/10.1016/j.epsl.2006.08.022
Hacker, B. R., and Christie, J. M., 1991, Observational evidence for a possible new diffusion path: Science, v. 251, n. 4989, p. 67–70, http://dx.doi.org/10.1126/science.251.4989.67
Holland, H. D., 1954, Radiation damage and its use in age determination, *in* Faul, H., editor, Nuclear Geology: New York, Wiley, p. 175–179.
Holm, D. K., Darrah, K. S., and Lux, D. R., 1998, Evidence for widespread ~1760 Ma metamorphism and rapid crustal stabilization of the early Proterozoic (1870-1820 Ma) Penokean Orogen, Minnesota: American Journal of Science, v. 298, n. 1, p. 60–81, http://dx.doi.org/10.2475/ajs.298.1.60
Hourigan, J. K., Reiners, P. W., and Brandon, M. T., 2005, U-Th zonation-dependent alpha-ejection in (U-Th)/He chronometry: Geochimica et Cosmochimica Acta, v. 69, n. 13, p. 3349–3365, http://dx.doi.org/10.1016/j.gca.2005.01.024
Hurley, P. M., 1952, Alpha ionization damage as a cause of low helium ratios: Transactions of the American Geophysical Union, v. 33, p. 174–183, http://dx.doi.org/10.1029/TR033i002p00174
——— 1954, The helium age method and the distribution and migration of helium in rocks, *in* Faul, H., editor, Nuclear Geology: New York, Wiley, p. 301–329.
Hurley, P. M., Larsen, E. S., Jr., and Gottfried, D., 1956, Comparison of radiogenic helium and lead in zircon: Geochimica et Cosmochimica Acta, v. 9, n. 1–2, p. 98–102, http://dx.doi.org/10.1016/0016-7037(56)90060-6
Ketcham, R. A., 2005, Forward and inverse modeling of low-temperature thermochronometry data, *in* Reiners, P. W., and Ehlers, T. A., editors, Low-temperature thermochronology: Techniques, interpretations, and applications: Reviews in Mineralogy and Geochemistry, v. 58, p. 275–314, http://dx.doi.org/10.2138/rmg.2005.58.11
Ketcham, R. A., Carter, A., Donelick, R. A., Barbarand, J., and Hurford, A. J., 2007, Improved modeling of fission-track annealing in apatite: American Mineralogist, v. 92, n. 5–6, p. 799–810, http://dx.doi.org/10.2138/am.2007.2281
Ketcham, R. A., Guenthner, W. R., and Reiners, P. W., 2013, Geometric analysis of radiation damage connectivity in zircon and its implications for helium diffusion: American Mineralogist, http://dx.doi.org/10.2138/am.2013.4249
Meesters, A. G. C. A, and Dunai, T. J., 2002, Solving the production-diffusion equation for finite diffusion domains of various shapes: Part II. Application to cases with α-ejection and nonhomogeneous distribution of the source: Chemical Geology, v. 186, n. 1–2, p. 57–73, http://dx.doi.org/10.1016/S0009-2541(01)00423-5
Meldrum, A., Boatner, L. A., Weber, W. J., and Ewing, R. C., 1998, Radiation damage in zircon and monazite: Geochimica et Cosmochimica Acta, v. 62, n. 14, p. 2509–2520, http://dx.doi.org/10.1016/S0016-7037(98)00174-4
Nasdala, L., Irmer, G., and Wolf, D., 1995, The degree of metamictization in zircon: A Raman spectroscopic study: European Journal of Mineralogy, v. 7, n. 3, p. 471–478.
Nasdala, L., Wenzel, M., Vavra, G., Irmer, G., Wenzel, T., and Kober, B., 2001, Metamictisation of natural zircon: Accumulation versus thermal annealing of radioactivity-induced damage: Contributions to Mineralogy and Petrology, v. 141, n. 2, p. 125–144, http://dx.doi.org/10.1007/s004100000235
Nasdala, L., Lengauer, C. L., Hanchar, J. M., Kronz, A., Wirth, R., Blanc, P., Kennedy, A. K., and Seydoux-Guillaume, A., 2002, Annealing radiation damage and the recovery of cathodoluminescence: Chemical Geology, v. 191, n. 1–3, p. 121–140, http://dx.doi.org/10.1016/S0009-2541(02)00152-3
Nasdala, L., Reiners, P. W., Garver, J. I., Kennedy, A. K., Stern, R. A., Balan, E., and Wirth, R., 2004a, Incomplete retention of radiation damage in zircon from Sri Lanka: American Mineralogist, v. 89, p. 219–231.
Nasdala, L., Gotze, J., Hanchar, J. M., Gaft, M., and Krbetschek, M. R., 2004b, Luminescence techniques in earth sciences, *in* Beran, A., and Libowitzky, E., editors, Spectroscopic methods in mineralogy: EMU Notes in Mineralogy, v. 6, p. 43–91.
Nasdala, L., Grambole, D., Gotze, J., Kempe, U., and Vaczi, T., 2011, Helium irradiation study on zircon: Contributions to Mineralogy and Petrology, v. 161, n. 5, p. 777–789, http://dx.doi.org/10.1007/s00410-010-0562-7
Rahn, M. K., Brandon, M. T., Batt, G. E., and Garver, J. I., 2004, A zero-damage model for fission-track annealing in zircon: American Mineralogist, v. 89, p. 473–484.
Reich, M., Ewing, R. C., Ehlers, T. A., and Becker, U., 2007, Low-temperature anisotropic diffusion of helium in zircon: Implications for zircon (U-Th)/He thermochronometry: Geochimica et Cosmochimica Acta, v. 71, n. 12, p. 3119–3130, http://dx.doi.org/10.1016/j.gca.2007.03.033
Reiners, P. W., 2005, Zircon (U-Th)/He thermochronometry, *in* Reiners P. W., and Ehlers, T. A., editors,

Low-temperature thermochronology: Techniques, interpretations, and applications: Reviews in Mineralogy and Geochemistry, v. 58, p. 151–179, http://dx.doi.org/10.2138/rmg.2005.58.6
Reiners, P. W., and Farley, K. A., 1999, Helium diffusion and (U-Th)/He thermochronometry of titanite: Geochimica et Cosmochimica Acta, v. 63, n. 22, p. 3845–3859, http://dx.doi.org/10.1016/S0016-7037(99)00170-2
Reiners, P. W., Brady, R., Farley, K. A., Fryxell, J. E., Wernicke, B., and Lux, D., 2000, Helium and argon thermochronometry of the Gold Butte block, south Virgin Mountains, Nevada: Earth and Planetary Science Letters, v. 178, n. 3–4, p. 315–326, http://dx.doi.org/10.1016/S0012-821X(00)00080-7
Reiners, P. W., Farley, K. A., and Hickes, H. J., 2002, He diffusion and (U-Th)/He thermochronometry of zircon: Initial results from Fish Canyon Tuff and Gold Butte: Tectonophysics, v. 349, n. 1–4, p. 297–308, http://dx.doi.org/10.1016/S0040-1951(02)00058-6
Reiners, P. W., Spell, T. L., Nicolescu, S., and Zanetti, K. A., 2004, Zircon (U-Th)/He thermochronometry: He diffusion and comparisons with $^{40}Ar/^{39}Ar$ dating: Geochimica et Cosmochimica Acta, v. 68, n. 8, p. 1857–1887, http://dx.doi.org/10.1016/j.gca.2003.10.021
Saadoune, I., Purton, J. A., and de Leeux, N. H., 2009, He incorporation and diffusion pathways in pure and defective zircon $ZrSiO_4$: A density functional theory study: Chemical Geology, v. 258, n. 3–4, p. 182–196, http://dx.doi.org/10.1016/j.chemgeo.2008.10.015
Salje, E. K. H., Chrosch, J., and Ewing, R. C., 1999, Is "metamictization" of zircon a phase transition?: American Mineralogist, v. 84, n. 7–8, p. 1107–1116.
Shuster, D. L., and Farley, K. A., 2009, The influence of artificial radiation damage and thermal annealing on helium diffusion kinetics in apatite: Geochimica et Cosmochimica Acta, v. 73, n. 1, p. 183–196, http://dx.doi.org/10.1016/j.gca.2008.10.013
Shuster, D. L., Vasconcelos, P. M., Heim, J. A., and Farley, K. A., 2005, Weathering geochronology by (U-Th)/He dating of goethite: Geochimica et Cosmochimica Acta, v. 69, n. 3, p. 659–673, http://dx.doi.org/10.1016/j.gca.2004.07.028
Shuster, D. L., Flowers, R. M., and Farley, K. A., 2006, The influence of natural radiation damage on helium diffusion kinetics in apatite: Earth and Planetary Science Letters, v. 249, n. 3–4, p. 148–161, http://dx.doi.org/10.1016/j.epsl.2006.07.028
Tagami, T., 2005, Zircon fission-track thermochronology and applications to fault studies, *in* Reiners, P. W., and Ehlers, T. A., editors, Low-temperature thermochronology: Techniques, interpretations, and applications: Reviews in Mineralogy and Geochemistry, v. 58, p. 95–122.
Tagami, T., Ito, H., and Nishimura, S., 1990, Thermal annealing characteristics of spontaneous fission tracks in zircon: Chemical Geology: Isotope Geoscience Section, v. 80, p. 159–169, http://dx.doi.org/10.1016/0168-9622(90)90024-7
Vermeesch, P., Sherlock, S. C., Roberts, N. M. W., and Carter, A., 2012, A simple method for in-situ U-Th-He dating: Geochimica et Cosmochimica Acta, v. 79, p. 140–147, http://dx.doi.org/10.1016/j.gca.2011.11.042
Watson, E. B., Wanser, K. H., and Farley, K. A., 2010, Anisotropic diffusion in a finite cylinder, with geochemical applications: Geochimica et Cosmochimica Acta, v. 74, n. 2, p. 614–633, http://dx.doi.org/10.1016/j.gca.2009.10.013
Weber, W. J., Ewing, R. C., and Wang, L.-M., 1994, The radiation-induced crystalline-to-amorphous transition in zircon: Journal of Materials Research, v. 9, n. 3, p. 688–698, http://dx.doi.org/10.1557/JMR.1994.0688
Williams, I. S., 2001, Response of detrital zircon and monazite, and their U-Pb isotopic systems, to regional metamorphism and host-rock partial melting, Cooma Complex, southeastern Australia: Australian Journal of Earth Sciences, v. 48, n. 4, p. 557–580, http://dx.doi.org/10.1046/j.1440-0952.2001.00883.x
Wolfe, M. R., and Stockli, D. F., 2010, Zircon (U-Th)/He thermochronometry in the KTB drill hole, Germany, and its implications for bulk He diffusion kinetics in zircon: Earth and Planetary Science Letters, v. 295, n. 1–2, p. 69–82, http://dx.doi.org/10.1016/j.epsl.2010.03.025
Worden, R. H., Walker, F. D. L., Parsons, I., and Brown, W. L., 1990, Development of microporosity, diffusion channels and deuteric coarsening in perthitic alkali feldspars: Contributions to Mineralogy and Petrology, v. 104, n. 5, p. 507–515, http://dx.doi.org/10.1007/BF00306660
Yamada, R., Murakami, M., and Tagami, T., 2007, Statistical modeling of annealing kinetics of fission tracks in zircon; reassessment of laboratory experiments: Chemical Geology, v. 236, n. 1–2, p. 75–91, http://dx.doi.org/10.1016/j.chemgeo.2006.09.002
Yund, R. A., Smith, B. M., and Tullis, J., 1981, Dislocation-assisted diffusion of oxygen in albite: Physics and Chemistry of Minerals, v. 7, n. 4, p. 185–189, http://dx.doi.org/10.1007/BF00307264
Yund, R. A., Quigley, J., and Tullis, J., 1989, The effect of dislocations on bulk diffusion in feldspars during metamorphism: Journal of Metamorphic Geology, v. 7, n. 3, p. 337–341, http://dx.doi.org/10.1111/j.1525-1314.1989.tb00601.x
Yurimoto, H., Morioka, M., and Nagasawa, H., 1989, Diffusion in single crystals of melilite: I. oxygen: Geochimica et Cosmochimica Acta, v. 53, n. 9, p. 2387–2394, http://dx.doi.org/10.1016/0016-7037(89)90360-8
Zattin, M., Picotti, V., and Zuffa, G. G., 2002, Fission-track reconstruction of the front of the northern Apennine thrust wedge and overlying Ligurian unit: American Journal of Science, v. 302. n. 4, p. 346–379, http://dx.doi.org/10.2475/ajs.302.4.346
Zhang, M., Salje, E. K. H., Capitani, G. C., Leroux, H., Clark, A. M., Schluter, J., and Ewing, R. C., 2000, Annealing of α-decay damage in zircon: A Raman spectroscopic study: Journal of Physics: Condensed Matter, v. 12, n. 13, p. 3131–3148, http://dx.doi.org/10.1088/0953-8984/12/13/321
Zhang, M., Salje, E. K. H., and Ewing, R. C., 2010, OH species, U ions, and CO/CO_2 in thermally annealed metamict zircon ($ZrSiO_4$): American Mineralogist, v. 95, n. 11–12, p. 1717–1724, http://dx.doi.org/10.2138/am.2010.3567